MINIATURE AUTONOMOUS ROBOTS FOR PIPELINE INSPECTION

A Thesis

by

WILLIAM TYLER MOSS

Submitted to the Office of Graduate and Professional Studies of
Texas A&M University
in partial fulfillment of the requirements for the degree of

MASTER OF SCIENCE

Chair of Committee,	James G. Boyd
Committee Members,	Raktim Bhattacharya
	Richard Malak
Head of Department,	Rodney Bowersox

December 2016

Major Subject: Aerospace Engineering

ABSTRACT

Aging natural gas pipeline infrastructure is becoming an increasingly large problem in the United States. There are more than 2.4 million miles of pipelines currently in use, all of which require regular maintenance and inspection to ensure safety. It is estimated that 70% of these lines were installed prior to the widespread use of the most common inspection tool, pigs, and therefore require some other tool to carry out tasks such as direct line inspection, pipeline mapping, gas quality monitoring, and cleaning. This has prompted a large growth in the area of robotic inspection devices to fill this market gap. However, many of the robots developed either fall short of true autonomy, are unable to operate in live flow conditions, or are designed for only a specific pipe size.

This thesis details the design of a robotic platform called MARPI, or Miniature Autonomous Robot for Pipeline Inspection, which addresses the weaknesses of both pigs and previous robots. MARPI is a wheeled robot that was developed to include several key features: energy harvesting, wireless communication, onboard navigation system, and a small profile and footprint in the pipe. The robot uses two 150:1 micro gear motors for its drive mechanism and features a permanent Neodymium magnet to make the robot adhere to the surface of steel pipes.

The energy harvesting system was characterized through a series of wind tunnel experiments which showed that to maximize the power generated it is best to have a turbine with a high number of buckets/blades, streamlined bucket geometry, and a relatively large offset from a bluff body below.

To carry out the design of MARPI, a statics model was developed and used to predict the magnetic force required to adhere to and avoid sliding in the pipe, and the motor torque required to propel the robot. This model was used to analyze the performance of the robot as a function of robot size. Key results show that to minimize power consumption, the robot should travel vertically with the flow, and to maximize range per day, a small robot with a large turbine is best.

ACKNOWLEDGEMENTS

I would like to thank my advisor, Dr. Boyd, for his guidance and support throughout the course of my research. Thanks also go to my friends and colleagues for making my time at Texas A&M University a great experience. I also want to extend my gratitude to the many undergraduate students whom I mentored over the past two years. I had a great time working with all of you and enjoyed having you on the team. Finally, thanks to my all of my family for their encouragement and support throughout my education.

TABLE OF CONTENTS

LIST OF FIGURES

LIST OF TABLES

1. INTRODUCTION

1.1 Background

It is estimated that there are 2.4 million miles of natural gas transmission and distribution lines in the United States. These pipelines provide energy access to more than 71 million customers, which accounts for nearly one-fourth of all energy consumed in the United States [1]. Naturally, maintaining functionality and safety of these pipelines through maintenance and inspection is a major concern, not only for the operators but also the government. However, nearly all of these pipelines are buried meaning there is restricted access and some sort of in-line inspection (ILI) tool must be used to carry out these tasks. In industry, the most commonly used tool is called a pig, or pipeline inspection gauge.

There are many types of pigs used, each of which has a specific task, either cleaning, fluid separation, or direct line inspection. Cleaning pigs often are mechanical in nature and are equipped with some form of brush or abrasive surface which scrapes off deposits on the inner surface of the pipe walls. There are also cleaning pigs which use chemical means to loosen these deposits from the walls so they can be removed easily by a second pig passing through. Plug pigs are used when there is a need to separate different fluid types to avoid mixing. To achieve direct line inspection pigs have been equipped with instruments such as calipers to measure diameter, or magnetic field sensors to detect wall thickness and metal loss. These are referred to as smart pigs and often incorporate several of the functionalities listed above. Examples of these pig types are shown in Figure 1-1.
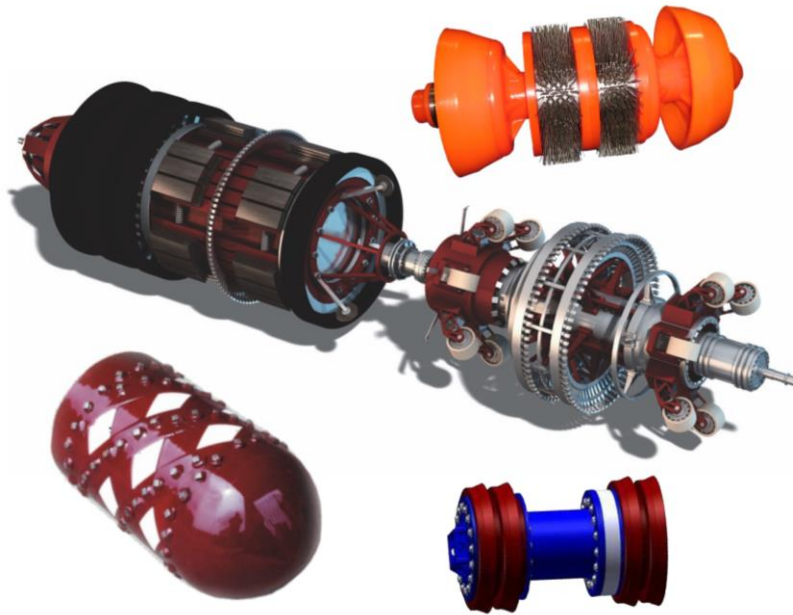
Figure 1-1: Various pig types including (from top to bottom) mechanical cleaning pig, smart pig, chemical cleaning pig, and plug pig. Image from [2].

There are several commonalities among all pig types. These include the fact that they are driven by the pressure differential existing in the pipe, are made to fit only a given pipe size, take up the entire cross sectional area, and lack nearly any degree of flexibility or means to navigate features that exist in all pipes such as bends, elbows, branches, or valves. Also, pigs are very expensive in terms of capital costs and labor to run and operate; it is estimated that it costs $35,000 per mile to operate intelligent pigs [3]. This cost comes not only from the device itself, but the launch/retrieval of the pig and preliminary evaluation of a pipelines piggability.

It is estimated that approximately 70 percent of natural gas transmission lines were constructed and installed before ILI devices, such as pigs, were commonly used in practice [1]. Therefore, most of these lines are said to be "unpiggable" meaning that they consist of small or varying diameters, tight bends, valves, or limited access. This fact along with

increasing federal safety regulations has prompted a large growth into research of new tools, specifically pipeline robots, to carry out tasks such as inspection, mapping, gas quality monitoring and cleaning.

1.2 Review of Pipeline Robots

There have been a large number of in-pipe robots proposed over the past two decades, all of which can be categorized by their mobility mechanism (Figure 1-2) and level of autonomy.
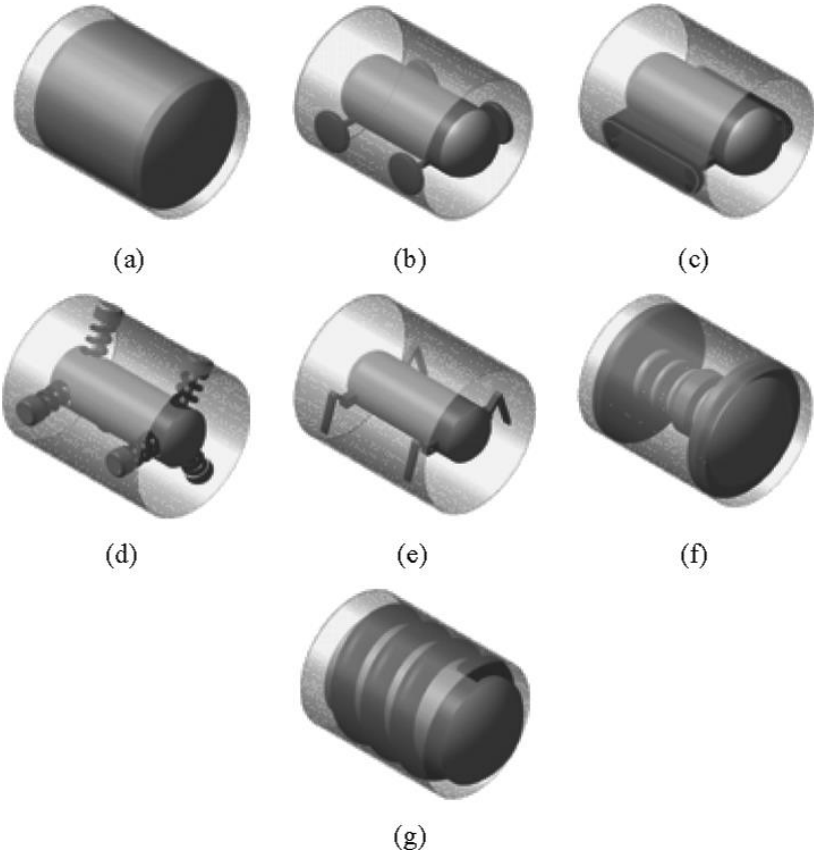
Figure 1-2: Classification of in-pipe robots. (a) Pig type. (b) Wheel type. (c) Caterpillar type. (d) Wall-press type. (e) Walking type. (f) Inchworm type. (g) Screw type. [4]

KANTARO [5] is an example of a fully autonomous wheel type robot. It was developed in Japan for inspection of sewer lines and uses lasers and a camera to autonomously navigate through pipes. Its angled wheels allow it to handle features such as bends or curves in the line. KANTARO was designed to operate in nearly empty sewage pipes with a diameter range of 200-300 mm.

Figure 1-3: KANTARO fully autonomous robot. Image from [5].

An example of an inchworm type robot is shown in Figure 1-4. This robot was developed by Brunete et al. [6] and achieves mobility via a series of 2 degree of freedom servomotors to achieve a snakelike motion. The robot was designed to travel in distribution lines larger than 40mm in diameter.

Figure 1-4: Modular micro robot. Image from [6].

A caterpillar type robot was developed by Kwon et al. [7] which consisted of two modules joined together by a spring and has silicone tracks powered by small DC motors to propel itself down the pipe. This robot utilizes a 4-bar linkage system to contract/expand its tracks to press fit into pipes ranging from 80-100 mm and is operated remotely via a tether link.
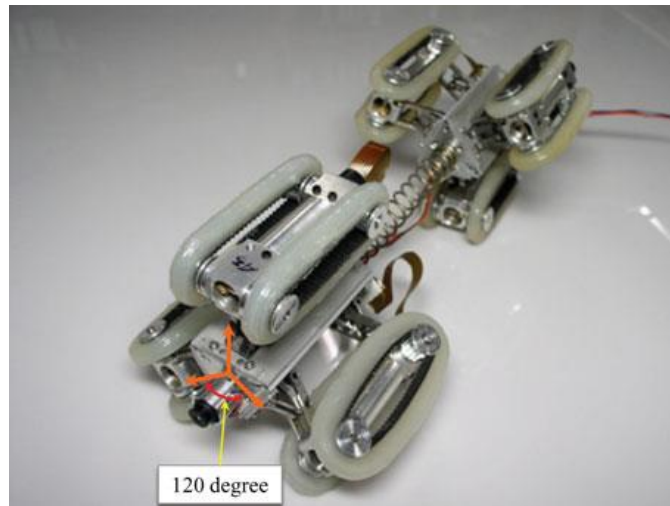
Figure 1-5: Caterpillar type robot proposed by Kwon et al. Image from [7].

The MRINSPECT series of in-pipe robots [4, 8, 9] are examples of robots which combine a wheeled and wall press method to achieve mobility. The latest development from this series is the MRINSPECT VI, which uses differential drive to steer the robot and introduces a transmission system to achieve independent speed control over all of the active wheels on the robot. MRINSPECT VI was designed to inspect 150 mm diameter gas pipes and is controlled by an outside operator via a tether.
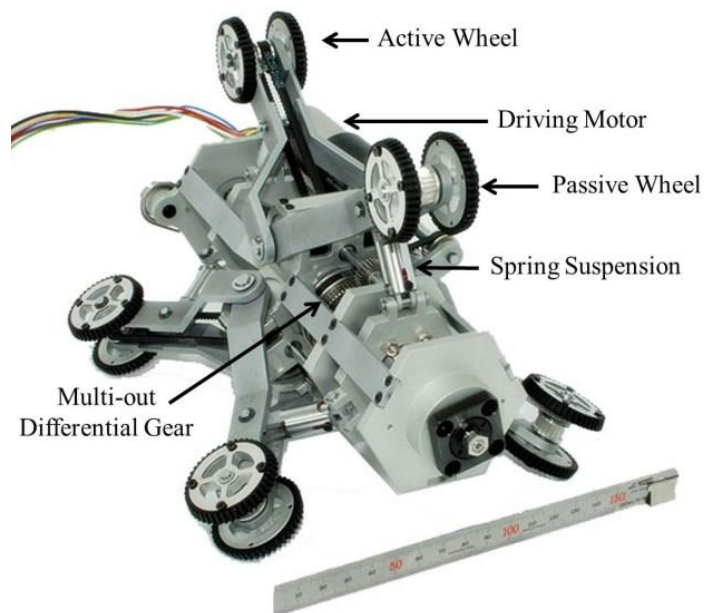
Figure 1-6: MRINSPECT VI in-pipe robot. Image from [9].

The RoboScan inspection robot is a conceptual modular snake-like robot developed by Foster-Miller and GE Oil & Gas under contract from the Northeast Gas Association. It was designed to perform direct in-line inspection of unpiggable natural gas lines while being controlled via a tether. RoboScan uses a unique "triad" mechanism to change its shape and adjust to features in the pipe as it propels itself inside the pipeline.

6
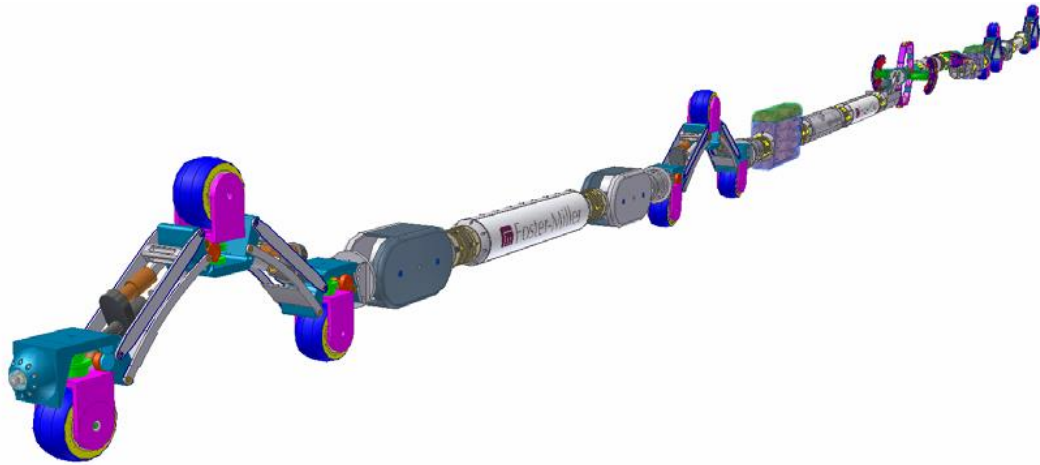
Figure 1-7: RoboScan inspection robot. Image from [10].

The Explorer family of robots by Pipetel Technologies [11] are examples of fully autonomous robots which are operable inside live pipelines. These robots are comprised of multiple modules joined together in series to form a snake-like body and have rigid arms with wheels to press against the wall as it propels itself down the pipeline. These robots are equipped with camera modules and sensors to detect metal loss and inner pipe surface deformation.
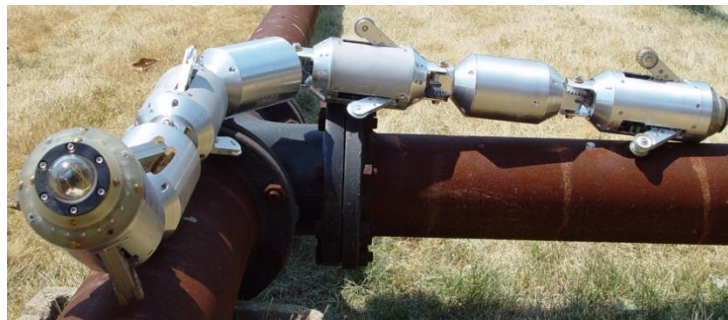
Figure 1-8: Prototype of the X-I Explorer robot originally designed at Carnegie Mellon University. Image from [12].

Many other wheeled [13], caterpillar [14], wall-press [15, 16, 17], walking, and

inchworm or snake-like [18] robots have been developed but are not fully covered here. A common feature of many of the robots reviewed is that most are designed for either a specific pipe size or small range of sizes and tend to take up a significant portion of the pipe cross sectional area. Also, because of either their large size or mobility mechanisms many of these robots are not capable of operation in live flow conditions. In addition, most robots commercially available and even those being developed utilize a tether system to address the issues of power, navigation, and communication. However, having a tether greatly restricts the access to entry points as well as the distance the robot can travel once inserted. Clearly cutting the cord alleviates these limitations, but it also poses new problems such as limited energy supply, autonomous navigation and control, storage and communication of sensor data, and potential failure and blockage of the line.

1.3 Thesis Objectives

The work in this thesis seeks to design and build a robotic platform which addresses the strengths and weaknesses of previously developed pipeline robots. This entails the development of a platform that has several key characteristics:

- A simple yet reliable mobility method which ensures the robot is capable of controlled movement within a live gas line without the risk of slippage or losing contact

- Ability to harvest energy from the surrounding environment and use this energy to charge onboard batteries

- Suite of sensors and processing capabilities to autonomously navigate in an unknown environment

8

- Ability to store and transmit data relevant to the desired ILI application

- Small profile and footprint to increase level of mobility through features such as valves, bends, and branches

1.4 Thesis Structure

The layout of this thesis is as follows. Section 2 presents the development of the equations governing the design and performance of a small pipeline robot using a force analysis. In section 3 the different subsystems of the robot are presented. This includes a discussion of functionality needed and proposed hardware solutions. Also the two different prototype robots built are reviewed. Section 4 introduces the energy harvesting experiments performed and presents the results for each. In section 5 a scaling analysis of the vehicle using MATLAB and the governing equations is outlined along with a discussion of the results. Finally, conclusions are drawn in section 6 along with a discussion of future work.

2. GOVERNING EQUATIONS

2.1 Pipe Flow

In order to model the robot, we must fully understand the flow inside of a pipe. First it must be determined if the flow is laminar or turbulent. In the case of highly pressurized natural gas pipe flow, the Reynolds number is typically on the order of 10^6 or higher, indicating turbulent flow. These high Reynolds numbers are due to the fact that natural gas has a low viscosity and relatively high density when compressed, as seen in Table 1.

Table 1: Data for an 18" compressed natural gas transmission line [10].

	Minimum	*Nominal*	*Maximum*
Centerline Velocity (m/s)	3.05	6.10	22.9
Pressure (kPa)	1720	2410	6900
Density (kg/m³)	19.5	23.5	72.0
Dynamic viscosity (cP)	0.0113	0.0121	0.0142

One way of modeling a turbulent flow profile, such as that shown in Figure 2-1, is by using the power-law velocity profile, which is an empirical expression that gives the fluid velocity as a function of radial position, r, from the centerline of the pipe. This relation is given by the following expression:

$$V_f(r) = V_{f,c}\left(1 - \frac{r}{R}\right)^{1/n}, \tag{1}$$

where $V_{f,c}$ is the centerline fluid velocity, R is the internal pipe radius, and n is a constant whose value depends on the Reynolds number. The value $n = 7$ or $n = 8$ is typically

chosen to approximate turbulent flows [19]. For the remainder of this thesis the value of $n = 8$ has been used.
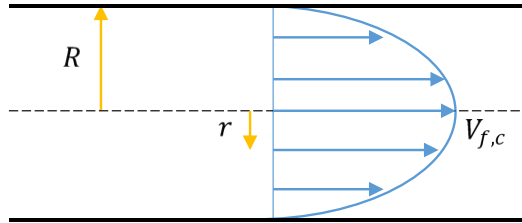
Figure 2-1: Pipe flow velocity profile.

2.2 Force Analysis

With the flow modelled we can now start to analyze the forces acting on the robot. Inside of a live pipe the forces acting on the robot would include: propulsive force (F_P), drag (F_D), gravity (mg), normal forces (N), frictional forces (F_{Fr}) and the magnetic force of attraction (F_{mag}). All of these forces are illustrated in Figure 2-2. In the case of a wheeled vehicle the normal forces and friction forces can be approximated as acting at a single point of contact at the bottom of the wheels. Therefore, the total friction force can be related to the total normal force acting on the robot using the following expression

$$F_{Fr} = F_{Fr_1} + F_{Fr_2} = \mu_s(N_1 + N_2), \tag{2}$$

where μ_s is the coefficient of static friction between the tires of the robot and the surface of the pipe. The drag force is a function of the flow acting over the entire robot and can be expressed as

$$F_D = \int_{r_t}^{R} \frac{1}{2} \rho C_D \vec{V}_{rel}^2(r) \, dA, \tag{3}$$

where r_t is the radial location of the turbine, ρ is the fluid density, C_D is the coefficient of drag, A is the frontal area, and $\vec{V}_{rel}$ is the relative velocity of the robot. The relative velocity can be expressed as

$$\vec{V}_{rel}(r) = \vec{V}_f(r) - \vec{V}_R, \tag{4}$$

where $\vec{V}_R$ is the robot velocity. In the case of an inspection robot it is ideal to have relatively small values of $\left|\vec{V}_R\right|$ (~ 0.2 - 0.5 m/s), as the goal is to take a sufficient number of readings from the local environment. In this study it is assumed that the flow of fluid in the pipe is always in the same direction and this is defined as the positive axial direction. Using these two points it can be stated that $\vec{V}_{rel}$ will always have a positive magnitude.
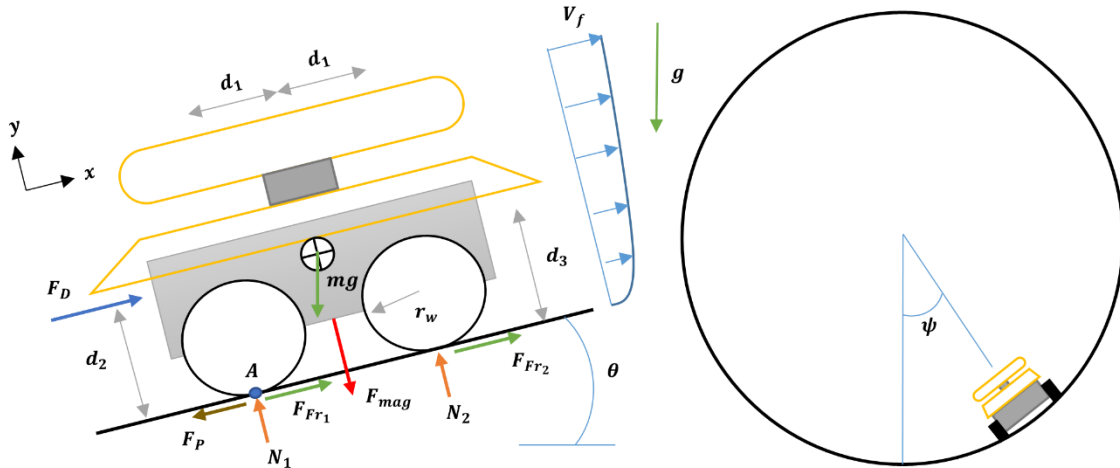
Figure 2-2: Free body diagram of robot in live pipe flow.

In Figure 2-2 d_1 is the distance between the wheel contact point and the center of gravity, d_2 is the distance between the wheel contact plane and the center of pressure, and d_3 is the distance between the contact plane and the center of gravity (c.g). By acknowledging the fact that the robot is nearly symmetric along its longitudinal axis and its cross sectional midplane, we can assume that the c.g lies at the geometric center and therefore d_1 is the same for each wheel. Furthermore, the magnet can be placed such that F_{mag} acts through the c.g to minimize asymmetry of the robot. The angles θ and ψ correspond to the inclination and circumferential orientation of the robot, respectively.

2.2.1 Statics Analysis

By using Figure 2-2 and statics, the following relations are obtained for the case when the robot is moving axially against the flow at constant velocity ($\vec{a} = 0$):

$$\Sigma F_x = 0: \qquad\qquad F_P = F_{Fr} + F_D - mgsin(\theta) \tag{5}$$

$$\Sigma F_y = 0: \qquad\qquad N_1 + N_2 = F_{mag} + mgcos(\theta)\cos(\psi) \tag{6}$$

$$\Sigma M_A = 0: \qquad N_2 = \frac{F_{mag}}{2} + \frac{F_D d_2}{2d_1} + \frac{mg}{2}\left[\cos(\theta)\cos(\psi) + \frac{d_3}{d_1}\sin(\theta)\right],$$
$$N_1 = \frac{F_{mag}}{2} - \frac{F_D d_2}{2d_1} + \frac{mg}{2}\left[\cos(\theta)\cos(\psi) - \frac{d_3}{d_1}\sin(\theta)\right] \tag{7}$$

Similar expressions are obtained for the case when the robot is moving axially with the flow at constant velocity ($\vec{a} = 0$):

$$\Sigma F_x = 0: \qquad\qquad F_P = F_{Fr} - F_D + mgsin(\theta) \tag{8}$$

$$\Sigma F_y = 0: \qquad\qquad N_1 + N_2 = F_{mag} + mgcos(\theta)\cos(\psi) \tag{9}$$

$$\Sigma M_A = 0: \qquad N_2' = \frac{F_{mag}}{2} - \frac{F_D d_2}{2d_1} + \frac{mg}{2}\left[\cos(\theta)\cos(\psi) - \frac{d_3}{d_1}\sin(\theta)\right], \tag{10}$$

13

$$N_1' = \frac{F_{mag}}{2} + \frac{F_D d_2}{2d_1} + \frac{mg}{2}\left[\cos(\theta)\cos(\psi) + \frac{d_3}{d_1}\sin(\theta)\right]$$

2.2.2 Design Requirements

In the case of designing an in-pipe robot, there are two major requirements to consider. These are the force needed to actively drive the robot, and the force needed to avoid losing contact or sliding due to the flow. In order to determine the magnetic force required we need to apply two constraints: the robot should not move without an active propulsive force ($F_p = 0$) and the wheels must maintain contact ($N_1, N_2 > 0$). These constraints must be met under the worst case conditions, i.e. maximum flow speed and drag acting parallel to $\vec{g}$ ($\theta = \pm 90°$). Substituting these conditions into (5) & (7) results in the following expressions:

$$F_{mag} \geq \frac{F_{D,max} + mg}{\mu_s},$$

$$F_{mag} \geq \frac{d_2}{d_1}F_{D,max} + \frac{d_3}{d_1}mg,$$

(11)

where $F_{D,max}$ is the maximum drag force which occurs at the maximum value of $\|\vec{V}_{rel}\|$. The maximum value of these two inequalities will now become a constant when studying vehicle design and performance.

The propulsive force, F_P, is defined as the force needed to actively move the robot. By combining (2) & (5)-(7) or (8)-(10) this force can be expressed as

$$F_P = F_D + \mu_s F_{mag} + mg[\mu_s \cos(\theta)\cos(\psi) - \sin(\theta)],$$

$$F_P = \mu_s F_{mag} - F_D + mg[\mu_s \cos(\theta)\cos(\psi) + \sin(\theta)],$$

(12)

14

depending on if the robot is moving against or with the flow, respectively. By analyzing

the forces acting on the wheels of the robot, the expression for the load torque placed on

each of the two driving motors is given as

$$\tau_M = F_P r_w / 2, \tag{13}$$

where r_w is the radius of the wheel.

From a design point of view, it is important to look at the limits of a system. One

such limit in this case is the maximum flow speed that can act on the robot before the

motors would stall. To ensure the robot is capable of handling any orientation we again

look at the worst case ($\theta = \pm 90°$, depending on robot heading with respect to flow). By

setting the load torque equal to the stall torque and combining (3), (4), (12) & (13) we

obtain the following expression:

$$V_{f,max} = \sqrt{\frac{2}{\rho A C_D}\left[\frac{2\tau_{stall}}{r_w} - mg - \mu_s F_{mag})\right] + V_R}$$

$$= \frac{2V_{f,c,max}\left(1 - \frac{r_t}{R}\right)^{1/n}}{R^2 - r_t^2}\int_{r_t}^{R}\left(1 - \frac{r}{R}\right)^{1/n} r \, dr, \tag{14}$$

where τ_{stall} is the stall torque rating of the motor. This maximum flow speed, $V_{f,max}$, is

equal to the average flow speed acting over the profile of the robot and can be related back

to the maximum allowable centerline velocity, $V_{f,c,max}$, by using (1) evaluated at the

turbine location, r_t. This relation can be used to quickly determine if a given robot design

is suitable for a given pipe size and/or flow rate.

15

2.3 Vehicle Performance

With the flow and forces acting on the robot analyzed, the vehicle performance can now be explored. For an inspection robot there are several key performance metrics of interest: the total power flow into and out of the battery, the maximum run time and range on one charge, and the recharge time.

2.3.1 Power Generated

The energy harvesting system is based on the conversion of kinetic energy from the flow, and therefore the following common expression for power produced by a wind turbine can be used:

$$P_g = \frac{1}{2}\rho\eta_{EH}A_tV_{rel}^3(r_t),$$
(15)

where η_{EH} is the efficiency of the energy harvesting system (turbine + generator), A_t is the swept area of the turbine, and $V_{rel}(r_t)$ is the relative velocity at the turbine. This power generated is the power flowing into the battery.

2.3.2 Power Consumed

The power out of the battery is that which is consumed by the electronics onboard the robot; namely the motors, microcontroller, shield and sensors. During normal operation it can be assumed that the microcontroller, shield and sensors will have relatively constant current draws which are given in their respective data sheets. However, the current draw from the motors is related to the load acting on the motor and is given by

$$I_M = \frac{I_{stall} - I_{free}}{\tau_{stall}}\tau_M + I_{free},$$
(16)

where I_{stall} and I_{free} are the stall current and no load current of the motor, respectively, and are parameters given by the motor manufacturer. In the case of a single inspection run (up to several hours) it is reasonable to assume that the flow will remain approximately constant and therefore it can be stated that the current draw from the motors will remain constant as well. Using the assumption of constant currents and the fact that voltage output of the battery is regulated, the power consumed by the robot can be expressed as

$$P_c = \sum_{i=1}^{N} \Phi_B I_i, \tag{17}$$

where Φ_B is the nominal voltage of the battery, I_i represents the current draw from a given component, and N is the total number of components.

2.3.3 Maximum Run Time & Range

By knowing how much power the robot will consume the maximum run time and range of the robot can now be determined. For a full charge these values are dependent on the amount of energy stored within the battery and the power flow into and out of the battery. They can be expressed as

$$t_{max} = DOD \times \frac{C_B \Phi_B}{P_c - P_g}, \tag{18}$$

$$Range_{max} = t_{max} |V_R|, \tag{19}$$

where C_B is the capacity of the battery in amp-hours (Ah), and DOD is the depth of discharge. The recommended depth of discharge for a LiPo battery is between 80 than 90 percent. This is to help prevent fatiguing the battery prematurely and avoid permanent

damage from severe depletion or overheating. For (18) to hold true it was assumed that the power generated is always less than the power consumed by the robot.

2.3.4 Charge Time

It is interesting to analyze not only the maximum range but also the additional range that the robot can travel for a given charge time. In order to do this, we assume that the robot has stopped and gone into an ultra-low power state performing nothing but harvesting energy for time, t_g. Now this newly generated energy is equivalent to the energy available for consumption,

$$E_g = P_g t_g = E_c = P_c t_c, \tag{20}$$

where t_c is the run time. Now combining (19) & (20) the following relation can be obtained:

$$Range = |V_R| \frac{P_g}{P_c} t_g. \tag{21}$$

It is clear from this equation that in order to maximize the range the robot can go for a given charge time; one would want to maximize the ratio P_g/P_c. Although an analytical expression for this ratio can be obtained using the equations presented in this thesis, it is preferable to show this relationship numerically since there are a multitude of variables at play simultaneously. This will be explored further in the vehicle scaling discussion in section 5.4.

The time to fully recharge the robot batteries is a similar expression to (18), but acknowledges the fact that the fastest way to do this is if the robot is consuming no power ($P_c = 0$). This results in the following expression for the time to obtain a full charge:

$$t_{full} = DOD \times \frac{C_B \Phi_B}{P_g}. \tag{22}$$

The range that the robot can travel in a one-day period can be calculated as a function of the maximum range per charge and the number of charge cycles in a day, as follows:

$$\frac{Range}{day} = Range_{max} \times (1 + \frac{24}{t_{full}}). \tag{23}$$

3. ROBOT OVERVIEW

On the proposed robotic vehicle there will be four major subsystems: mobility, energy harvesting, navigation, and communication. This section gives a background and draws conclusions on the functionality and hardware of each subsystem.

3.1 Mobility

3.1.1 Mobility Mechanism

One of the biggest considerations when designing a mobile robotic platform is the actual mechanism by which it achieves its mobility. In the case of robots intended for pipeline inspection this is most often in the form of wheeled arms which actively press against the wall to maintain contact and therefore a tractive force. This mechanism along with other types such as crawlers, walking, or inchworm like robots frequently have many failure points and require a large number of actuators. As miniaturization and the limited power supply were of key importance in this research, it was decided to create a wheeled type robot.

3.1.2 Motor Selection

The key concern when determining if a robot will be able to achieve mobility inside of a live pipeline is the maximum loading its actuators can handle. For small robotics the most common actuator is a DC motor and this limit is defined as the stall torque, τ_{stall}. While the stall torque is a driving factor which must be satisfied, there are more factors to consider when selecting the best DC motor for the job. These include: desired operating speeds, voltage rating, current draw, and efficiency. In the case of an inspection robot, it is important to allow ample time for the inspection sensors to take

readings from the local environment. Therefore, desired operating speeds are relatively slow and the ability to achieve high speeds is of little importance when selecting motors. Since there is a limited amount of energy available, minimizing the current draw is very important concerning battery and mission lifetime.

To fully understand motor performance, the equations governing the previously mentioned parameters must be defined. The motor loading and current draw have already been presented in (13) and (16) respectively. The expression for the motor rotational speed is similar to that of the current draw and is given as

$$\omega_M = -\frac{\omega_{free}}{\tau_{stall}}\tau_M + \omega_{free},$$ (24)

where ω_{free} is the rotational speed of the motor when no load is applied. Using the metrics of stall torque, current draw, rotational speed, linear speed, power output, and efficiency, it was decided to use 150:1 high power micro metal gearmotors. The performance of this motor over the expected torque loads is shown in Figure 3-1.
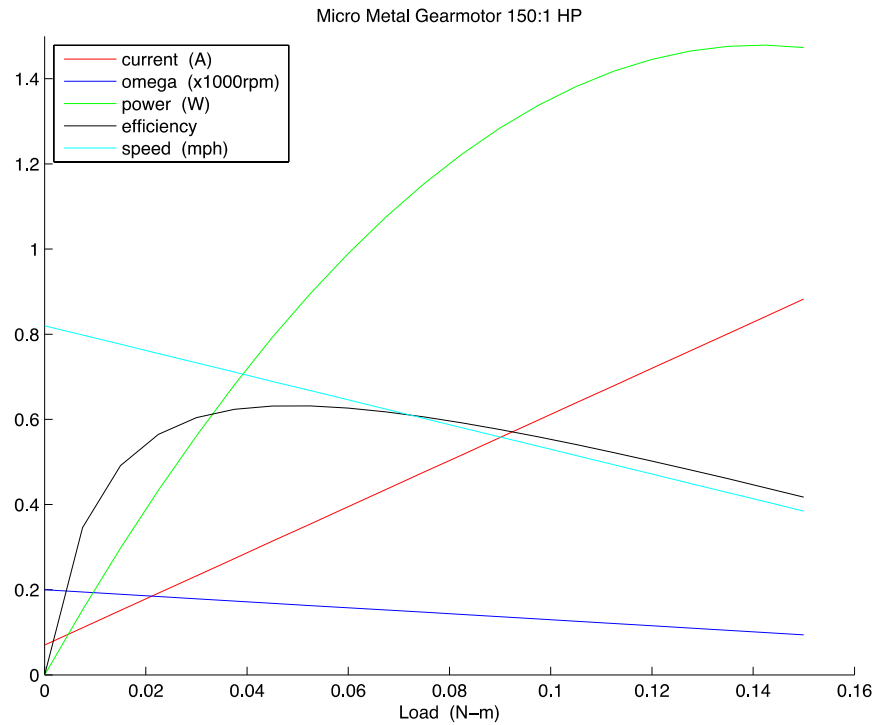
Figure 3-1: Performance curves for the 150:1 high power micro metal gearmotor.

It is important to note that due to the stall torque requirement from the maximum motor loading, the amount of variety of motors was very limited. It was a necessity to have a high gear ratio to handle these loads and the series of micro metal gearmotors available from Pololu Robotics & Electronics offered virtually the only viable option.

3.1.3 Magnetism in Robots

While actuators are ultimately the limiting factor in mobility, there still needs to exist a mechanism to ensure that the robot wheels do not lose contact and that the robot is not blown downwind by the fluid flow. As a majority of gas lines in service, especially older unpiggable lines, are made of steel, magnetism is a reliable option that can passively address these problems.

There have been a number of previous robots which use the convenience of permanent magnets to achieve similar goals as those presented here. These mechanisms range from a collection of small magnets embedded in the tracks (Figure 3-2) or wheels (Figure 3-3), large magnetic wheels (Figure 3-4), or simply a large magnet on the underside of the body (Figure 3-5). From these mechanisms it was determined that the most suitable option for the proposed work was to use a single magnet on the underside of the robot. By placing the magnet in the center of the bottom plane, not only would this help to create a symmetric robot, but also to evenly distribute the pull force of the magnet across all wheels.

Figure 3-2: Magnetic track developed for the robot SIRUS [20].

Figure 3-3: Pipe inspection robot developed by Honeybee Robotics [21].
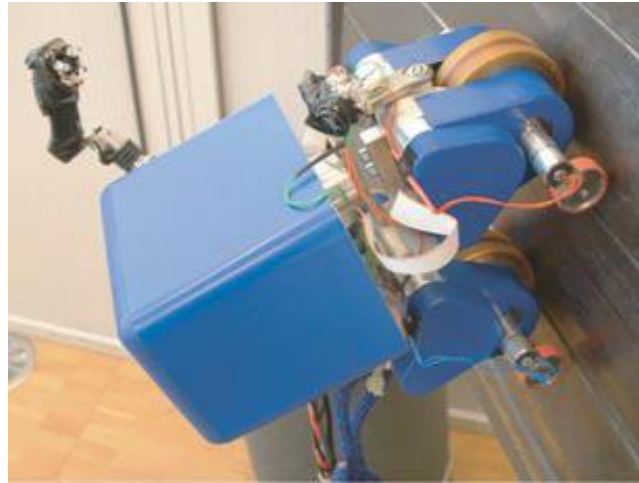
Figure 3-4: Magnebike robot featuring large magnets at the core of its wheels [22].

Figure 3-5: FerroTanker-20 robot featuring a large magnet under its body [23].

3.1.4 Magnet Sizing

In order to determine the size and strength of magnet needed the design requirements set forth in (11) were used. But first, the fact that the robot will operate inside a circular pipe must be addressed. In order to account for this curvature, a simple geometric

24

relation called a chord and trigonometry can be used. A chord is any straight line that connects two points on a circle. In the case of this robot, several variables would be known such as the overall robot width (w), and the pipe internal diameter (D) and radius (r). These are illustrated in Figure 3-6. The unknown variables, the chord (c) and distance from the pipe surface to where the magnet would be placed (h), can be found by using the following relations:

$$\theta = \sin^{-1}(w/D)$$

$$c = D\sin(\theta/2)$$

$$h = \sqrt{c^2 - (w/2)^2}$$

(25)

With this distance, h, now known, a tool is needed to determine the magnetic pull force between a magnet and a steel surface. For this work the online magnet calculator by K&J Magnetics [24] was used. Their online calculator is based on experimental testing using their range of neodymium magnets and can account for various magnet geometries, grades, and dimensions. This calculator was used to arrive at the minimum size and grade of magnet required for a given distance, h. This site was also used to purchase all magnets used in this research.
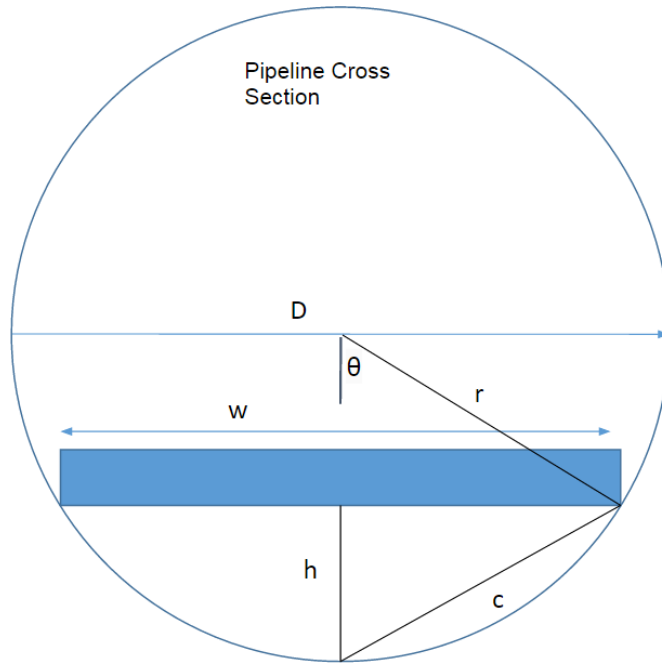
Figure 3-6: Geometry used for determining magnet size required.

3.2 Energy Harvesting

3.2.1 Background

The addition of an energy harvesting system is key in realizing a truly autonomous robot. However, this is not a problem where there is a one size fits all solution. It depends largely on the application and the operating environment. The first thing to consider is the types of energy available. This can be in the form of electromagnetic, thermal, mechanical or chemical energy. While all of these energy types have different working principles determining exactly how much of each type is available, they are all based on the same physical principle, the conservation of energy. The conservation of energy is given as

$$\dot{KE} + \dot{PE} + \dot{U} = \dot{Q} + \dot{W}, \tag{26}$$

where KE, PE, and U represent the kinetic, potential, and internal energy of the system, respectively; Q is the heat gained by the system; W is the work done on the system; and

26

the dot notation indicates the rate at which these quantities are changing. In nearly all cases energy harvesting involves converting energy from one type to another which is in turn used as a power source. Table 2 summarizes the operating principles and lists a few possible devices for each type of energy.

Table 2: Operating principles and common devices for each energy type

Type of Energy	Operating Principles	Possible Devices
Electromagnetic	Light capture, induction	Solar cell, RF wave harvester, inductor
Thermal	Temperature gradient	Thermoelectric generator, pyroelectrics
Mechanical	Movement (vibration, wind/tidal current), stress, strain	Turbine, piezoelectrics, vortex capture device, pressure diaphragm
Chemical	Chemical reaction	Fuel cell, combustion engine

3.2.2 Design Selection

In the case of a natural gas pipeline the only appreciable amount of energy comes in the form of mechanical energy due to the fluid flow and chemical energy from the gas itself. However, it could be quite dangerous to use the natural gas itself as a fuel in a combustion process and therefore any sort of chemical burning engine was not considered. The only other real option to harvest chemical energy is in the form a fuel cell, the development of which is outside of the scope of this thesis. Therefore, only devices capable of harvesting mechanical were considered. These included vortex capture devices, piezolectrics, and turbines.

Vortex capture devices are based on the flow over a body creating a vortex behind it, which is then used to either oscillate the body itself or a flexible structure behind it. One such application of this is used in harvesting energy from underwater currents. This type

of device has some sort of fixed point and can either be fixed or freely suspended on the other end. As the fluid flows around the body, vortices form behind it and cause the body to oscillate vertically. This motion can be harvested by either a linear actuator or piezoelectric generator. Another example of this type of device is one which has a flexible tail behind the body which is free to move, similar to a flag in the wind. This tail is usually made of piezoelectric material so that the continuous flexion/tension generates electrical energy. Examples of these two types of vortex capture devices are shown in Figure 3-7.
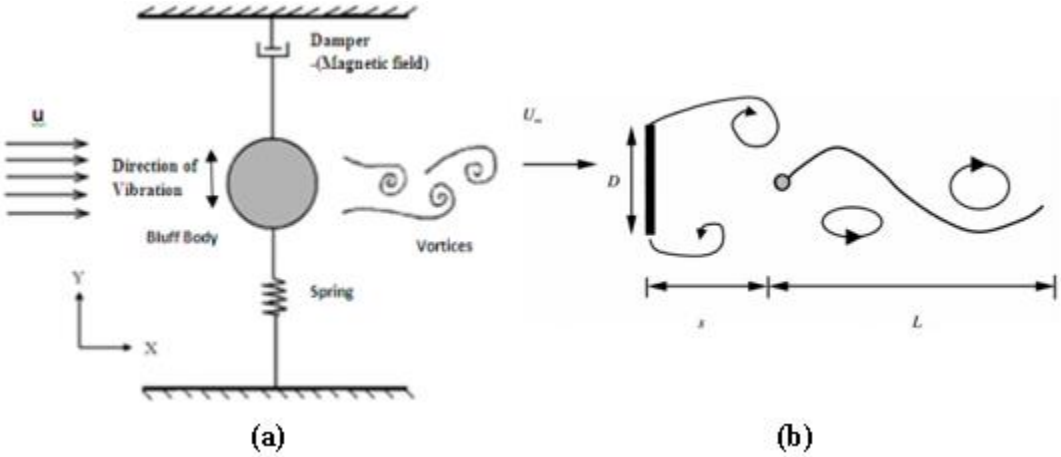
**Figure 3-7: (a) Bluff body vortex capture device proposed by Lobo et al. [25].
(b) Piezoelectric "eel" vortex capture device proposed by Allen et al. [26].**

There are also devices which utilize a pressure chamber to create a pressure differential as a fluid is flowing. This pressure differential actuates a piezoelectric diaphragm which converts the mechanical energy into electrical energy. An example of this device is shown in Figure 3-8.
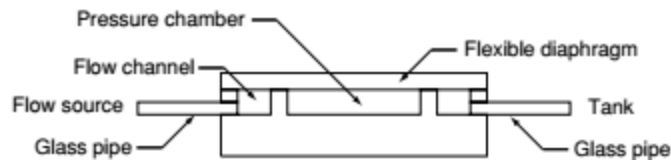
Figure 3-8: Piezoelectric energy harvester proposed by Wang et al. [27].

Turbines can be grouped into two main categories: horizontal axis turbines (HATs) and vertical axis turbines (VATs). The horizontal/vertical axis here refers to the axis on which the turbine rotates, either parallel with the ground (horizontal) or perpendicular to the ground (vertical). Within these two categories are many different turbine designs, such as those shown in Figure 3-9. Horizontal axis turbines are more commonplace in the wind power industry due to the fact that they typically will produce more electricity for a given wind speed compared to VATs. However, VATs have their niche in the small wind market as they perform better in turbulent wind conditions as they are generally omnidirectional, meaning they can harvest energy with fluid coming in from any direction. Also, VATs can have a lower height profile while maintaining a large swept area compared to HATs. Regardless of the type of turbine, they often suffer from several issues as they are scaled down. These issues are decreased efficiency and power generation, and worse startup characteristics. The poor startup performance is exacerbated by the fact that generators do not scale down exceptionally well either. However, it is still possible to scale down turbines as long as there is special consideration to the design and hardware used.
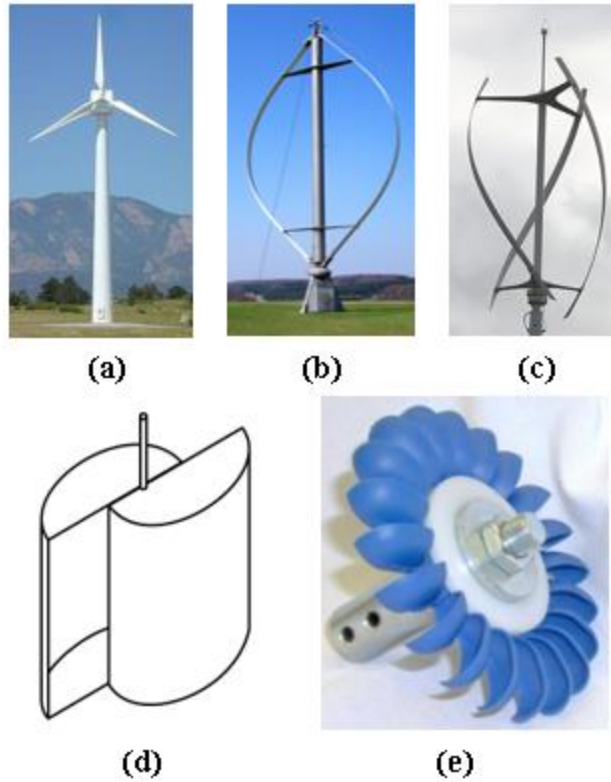
Figure 3-9: Various turbine types: (a) modern HAT (b)Darrieus VAT (c) Gorlov VAT (d) Savonius VAT (e) Pelton wheel.

As mentioned previously, turbines are based on capturing the mechanical energy from the flow. The mechanical power available in a fluid flow can be obtained using (26) and results in the following expression, assuming no losses due to heat:

$$P = \dot{W} = \dot{KE} = \frac{1}{2}\rho A V_f^3 \tag{27}$$

where ρ is the fluid density, A is the swept area of the turbine, and V_f is the fluid velocity. While turbines suffer from scaling issues, the level of power they generate (mW-kW) [28] is often several order of magnitudes higher compared to piezoelectric devices (nW-mW) [27]. For this reason, it was decided to use a turbine as the energy harvesting mechanism. When comparing the different types of turbine designs, it was decided to use a design

based on a Pelton wheel which is a type of vertical axis turbine. This design permits omnidirectional energy harvesting while allowing the robot to maintain a low profile within the pipe. Also this style of turbine typically has relatively high performance at small scales compared to others.

Initially it was considered to utilize a diffuser in the energy harvesting system to try and increase the flow speed into the turbine. The ability to do so could drastically increase the power generated given that the power level scales with V_f^3. Several different diffuser housings were built and tested, but ultimately it was decided to move forward without any sort of diffuser. The small scales did not translate well in effectively increasing the flow rate and only made the poor starting performances at small sizes worse.

3.2.3 Special Considerations

The decision to use a turbine as the energy harvesting mechanism brings other considerations with it, namely the fact that turbines output mechanical energy. Therefore, an electric generator is needed to convert this into electrical energy. When considering a generator meant to charge a battery, it is desirable to produce high voltages at low rotational speeds. For DC motors/generators this is defined by what is known as the voltage constant, or K_V, which has units of RPM/Volts. This means to generate high voltage it is desirable to have a low K_V. However, a low K_V motor is typically larger since to achieve this requires more internal windings or a more complex winding pattern. As the size of the generator increases its inertia is increased meaning a larger torque is required to start and continue spinning the shaft. This increase in startup torque can be detrimental when trying to harvest energy from a fluid flow as it directly relates to the cut-in speed, or

the speed at which the system will begin to generate energy. As the flow is limited in nearly all applications, it is important to have this cut-in value relatively low compared to the range of expected flow speeds. Therefore, when selecting an electric generator, it is important to find a good balance between K_V and startup torque.

Not only must this system produce electrical energy, but it must be capable of conditioning this energy into a form acceptable to charge the onboard batteries. This means that the system must be capable of producing an output of a constant voltage above the nominal voltage of the batteries used. For this research lithium polymer (LiPo) batteries were used, which have a nominal voltage of 3.7 V. The use of LiPo batteries was based on the fact that they provide a very high energy density, low self-discharge rate, and high life span relative to other battery types. Using this information, it was determined that the robot needed to include a voltage regulator and an IC meant for charging LiPos.

3.3 Navigation

3.3.1 Introduction

In order to realize an autonomous robot, it must be capable of determining information about where it is, where it has been, and where it is going. This requires knowledge of what is called a state vector, which in this case would be $(\vec{x}, \vec{v}, \vec{a}, \theta, \psi, \beta, \dot{\theta}, \dot{\psi}, \dot{\beta})$. Here $\vec{x}, \vec{v}$, and $\vec{a}$ represent the position, velocity, and acceleration vectors of the vehicle, respectively. The angles θ, ψ, and β represent the pitch, roll, and yaw angles of the body with respect to a given coordinate frame, and the rates of each of these angles is given by $\dot{\theta}, \dot{\psi}$, and $\dot{\beta}$, respectively. In order to fully and accurately determine all of these values a robot would need to be outfitted with a variety of different

navigational sensors. The most common solution to this problem is through the use of an inertial measurement unit (IMU) combined with a global positioning system (GPS). An IMU typically contains both a 3-axis accelerometer, which measures linear accelerations, and a 3-axis gyroscope, which measures angular velocities. These values are then integrated in time to obtain an estimation as to the velocity, position, and orientation of the body. However, IMUs are prone to both short term noise in the signal and long term drift due to the integration and accumulation of possible errors. These shortcomings are where GPS comes in as it can provide the navigation computer with reference values that can be used to mitigate the errors.

Since the work in this thesis is to build a robot which operates inside of a steel pipe, a GPS based device cannot be used as the electromagnetic waves that provide the signal to the GPS receiver cannot penetrate steel. This requires that an alternative method of navigational sensing be used. Possible alternative sensors include odometers/encoders, pressure sensors, ultrasonic sensors, infrared sensors, or visual sensors. Due to the size and power limitations placed on the robot, the physical size of each component, power consumption, accuracy, and computational processing required are important factors in determining the final solution.

3.3.2 Proposed Solution

The proposed navigation solution is to use a combination of a 3-axis accelerometer, optical encoders, and piezoelectric pressure sensors.

As mentioned before, a 3-axis accelerometer measures the linear accelerations in 3 principal axes (see Figure 3-10). Accelerometers are often used in devices such as smart

phones, tablets, drones, and even planes for a variety of uses. This could be as simple as screen rotation as the devices orientation is changing, or as sophisticated as providing flight stabilization.
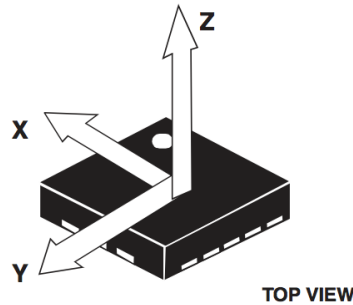
Figure 3-10: Accelerometer coordinate system showing 3 principal axes.

For the purposes of this robot, the accelerometer will be used to aid in determining the roll and pitch angles of the robot inside the pipe. The way it can do this is due to the fact that accelerometers measure the proper acceleration, or the true acceleration of an object including gravity. The fact that gravity is always present, means it can then be used as a reference to determine these angles. The different coordinate frames considered here are the inertial coordinate frame, pipe coordinate frame, and robot coordinate frame. The inertial coordinate frame (see Figure 3-11) is a Cartesian coordinate system that uses the gravity vector as a reference to be defined. The pipe coordinate frame (see Figure 2-2) is a cylindrical coordinate system that is defined by using the direction of the gas flow within the pipe. The robot coordinate frame is a body fixed frame on the robot which is defined by the accelerometer principal axes and its placement on the robot.
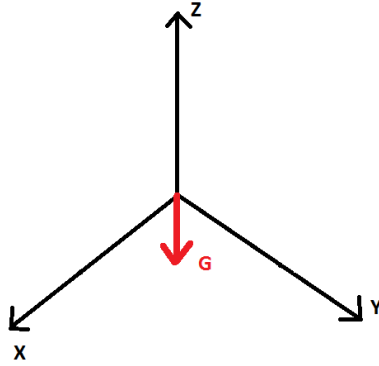
Figure 3-11: Inertial reference frame.

These three frames can be related by considering a sequence of coordinate transformations using the yaw, pitch, and roll angles of the robot. An example of these transformations for each rotation is shown in Figure 3-12. By knowing the sequence in which these rotations occur, simple matrix math can be used to determine the final relations in terms of the three angles. For this work a 3-2-1, or yaw-pitch-roll, sequence was used. Using this sequence and by referencing the gravity vector, the following expression shows the final relation between the values measured by the accelerometer and the pitch and roll angles:

$$\begin{bmatrix} a_x \\ a_y \\ a_z \end{bmatrix} = \boldsymbol{R}_x(\psi)\boldsymbol{R}_y(\theta)\boldsymbol{R}_z(\beta) \begin{bmatrix} 0 \\ 0 \\ -1 \end{bmatrix} = \begin{bmatrix} \sin(\theta) \\ -\cos(\theta)\sin(\psi) \\ -\cos(\theta)\cos(\psi) \end{bmatrix} \tag{28}$$

Using this expression, the pitch and roll angles, θ and ψ respectively, are calculated as:

$$\theta = \sin^{-1}(a_x), \qquad \psi = \tan^{-1}(\frac{a_y}{a_z}). \tag{29}$$

35
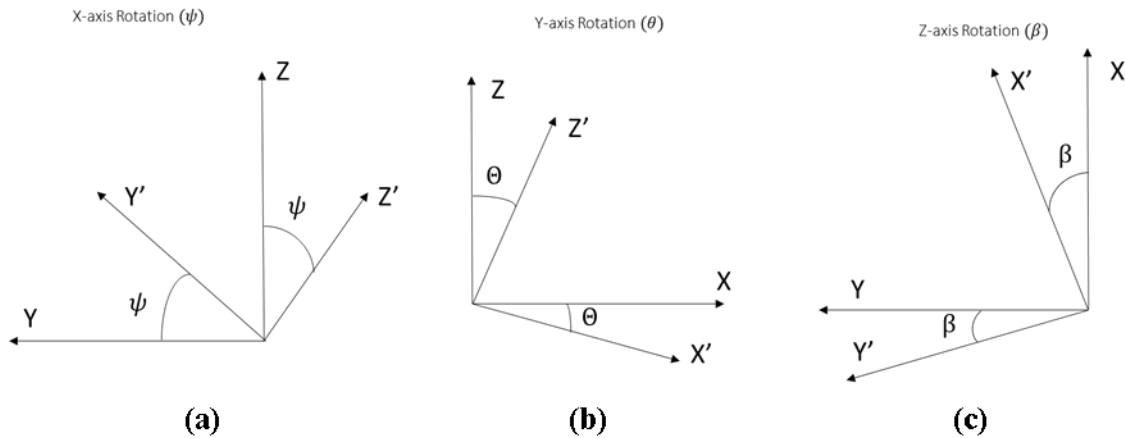
Figure 3-12: Example coordinate transformations (a) roll about x-axis by ψ (b) pitch about y-axis by θ (c) yaw about z-axis by β.

It is important to note that there are numerous sources of error associated with accelerometers that could affect the accuracy of this solution. These errors include static bias, signal noise, drift due to temperature, and drift over time. Static bias error is simply a possible constant offset from the true value and can be accounted for through proper sensor calibration. Static bias values for all three principal axes are often given in product datasheets and only a simple addition or subtraction is needed to correct readings for this type of error. Noise is something that is always present in sensors and represents a random deviation around the true reading of the sensor. Manufacturers often will list the noise in an accelerometer as an amplitude in units of $\mu g/\sqrt{Hz}$. To address noise a common practice is to use a low pass filter or Kalman filter in the controller, which characterizes the noise and adjusts the readings to increase the accuracy of the final output. Temperature can also have a large impact on accuracy, as the sensitivity, static bias, and noise density all change with the temperature. Again, the effect of temperature on these values is often characterized by the manufacturers and provided in product data sheets. Therefore, by

36

adding the proper expressions in the control program these effects can be accounted for. The typical long term drift associated with using accelerometers in navigation systems comes from the fact that the raw acceleration values, which suffer from static bias and noise, are integrated in time to obtain an estimation of velocity and position. This integration only compounds these errors and can lead to the solution becoming quickly incorrect. However, the proposed solution uses the instantaneous accelerometer readings to estimate the pitch and roll angles through geometry and therefore drift due to averaging over time is a non-issue. In addition, any non-zero linear acceleration could lead to possible errors. However, it is envisioned that the robot will maintain an approximately constant travel speed as it carries out its inspection tasks within a pipeline. Therefore, it is assumed that on average, there will be little to no effect of non-zero accelerations on the readings. This concern is further lessened by the fact that the task of taking these readings and calculating these values requires very little computation time and can therefore be performed at a high frequency.

To obtain the last needed angle, the yaw angle β, piezoelectric pressure sensors will be used. The way this will be done is by measuring the dynamic pressure levels at four different points on the robot (see Figure 3-13). These values can be compared with each other and amongst a calibrated table of reference data to determine the exact heading angle of the robot with respect to the gas flow, or simply the yaw angle.
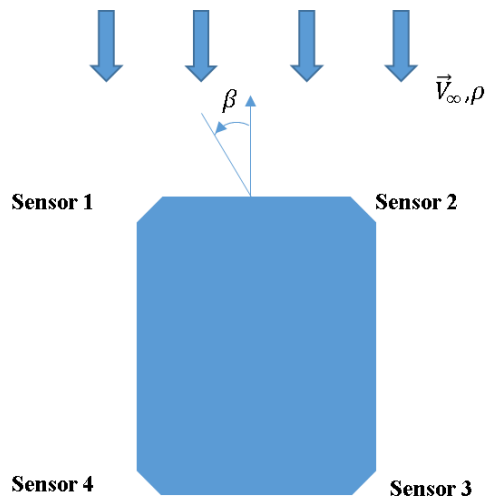
Figure 3-13: Pressure sensor placement on robot.

The rationale here is that based on the placement of the sensors, there will always be at least 2 sensors reading a dynamic pressure of zero, or just ambient pressure. By knowing the analog values of all pressure sensors, those reading zero dynamic pressure can be determined. From this point, the controller can determine which quadrant the vehicle is oriented in, according to Table 3, and even an estimation of the exact angle. A flowchart summarizing the logic of this process is shown in Figure 3-14.

Table 3: Case definitions to determine quadrant of yaw angle. X indicates a non-zero dynamic pressure reading.

Case	β	Sensor 1	Sensor 2	Sensor 3	Sensor 4
1	$45 \leq \beta \leq 135$	Ambient	x	x	Ambient
2	$135 \leq \beta \leq 225$	Ambient	Ambient	x	x
3	$225 \leq \beta \leq 315$	x	Ambient	Ambient	x
4	$315 \leq \beta \leq 360$ OR $0 \leq \beta \leq 45$	x	x	Ambient	Ambient

38
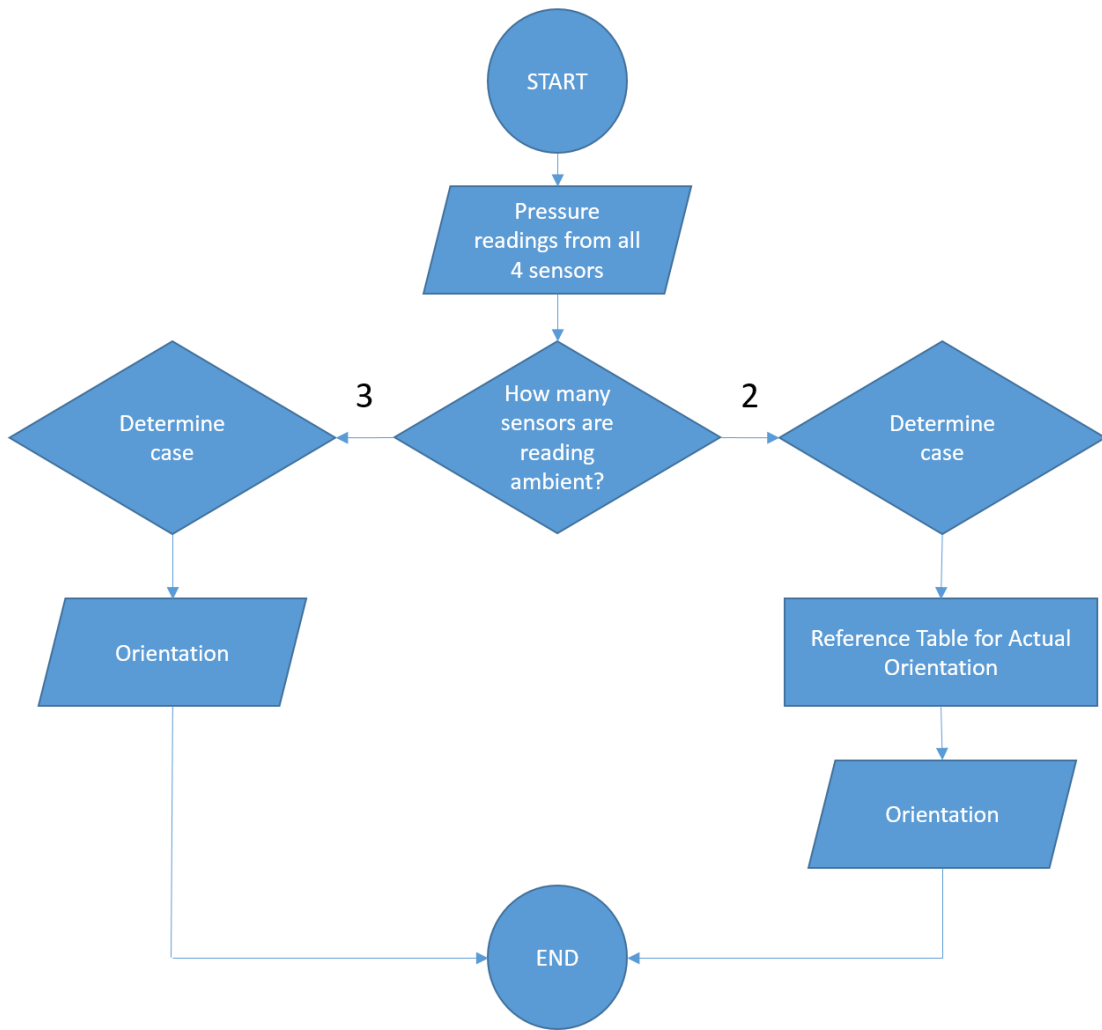
Figure 3-14: Flowchart of logic to determine robot orientation w.r.t flow.

In order to calculate the exact angle, it is important to understand how piezoelectric pressure sensors operate. When a stress is applied to a piezoelectric crystal, it produces a voltage through the piezoelectric effect. This voltage can be quantified using the crystal properties and the stress being applied to it, which can be expressed in terms of flow speed and incidence angle, as

$$\Phi_{pe} = -\frac{t}{2} g_{33} \rho V^2 \sin^2 \beta, \tag{30}$$

where Φ_{pe} is the output voltage, t is the crystal thickness, g_{33} is a piezoelectric material constant, ρ is the fluid density, V_∞ is the fluid speed, and β is the yaw angle of the robot. This voltage is then sensed by analog voltage meters on the microcontroller and referenced to a table of calibrated data.

Note that in Figure 3-13 the sensors are set at 45° angles rather than directly on the front or side faces of the robot. This was done to maximize the sensitivity of the sensors around the extremes, which occur at multiples of 90°. The idea here is that the robot will likely spend a majority of its time moving axially within the pipe ($\beta = 0°, 180°$) and therefore offsetting the sensors from being directly in line with the flow is best. An example output demonstrating this behavior is shown in Figure 3-15. Note that the sensitivity of a sensor at any given heading angle is simply the slope at that point.
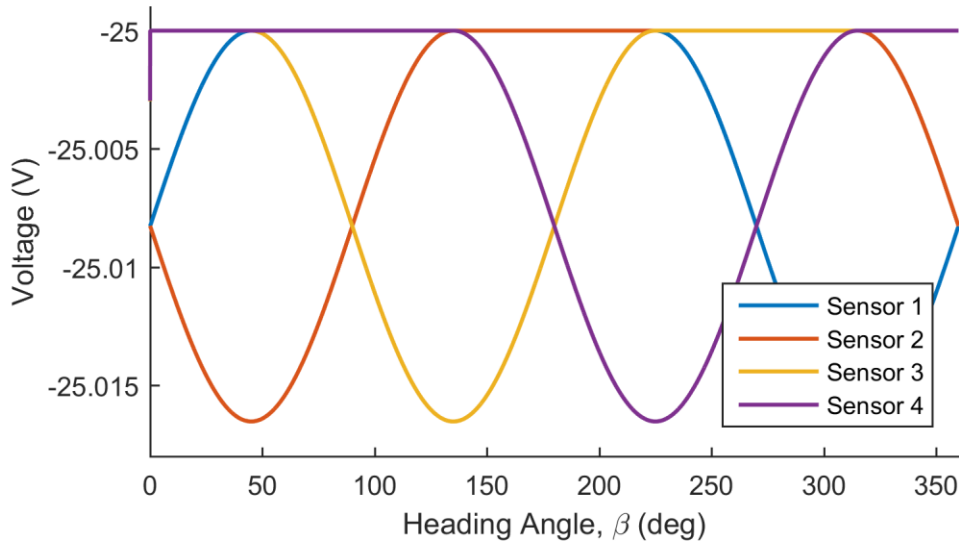
Figure 3-15: Example output of piezo pressure sensors.
$$g_{33} = 25 \times 10^{-3}\,\frac{V\,m}{N}, \ \rho = 23.5\,\frac{kg}{m^3}, \ V_f = 7.5\,\frac{m}{s}.$$

The last sensor needed to obtain a full navigation solution is an optical encoder. Optical encoders measure the number of times an object blocks light passing into a photodiode and are often attached in some way to a shaft. They are used to determine how far a shaft has rotated, which in turn can be related to distance travelled. Encoders can also be used to obtain the robot velocity, assuming an accurate clock is available, by counting the rotations of the shaft per unit time. Fortunately, there is a wide variety of encoders available, even ones designed to be paired with the micro metal gearmotors that are currently used on the robot. Figure 3-16 shows one such motor with an optical encoder mounted on a secondary shaft on the back end.

Figure 3-16: Optical encoder available from Pololu Robotics & Electronics [29].

The limitation of using encoders is based on their ability to accurately count the passes of the wheel as the motor shaft is spun. This is given by their sensitivity, which is given in counts per revolution. This value can be used in combination with the gear ratio of the motor and the radius of the wheel to obtain an algebraic expression relating the counts by the encoder to the linear distance travelled. In addition, by having an encoder on each wheel, the vehicle can accurately track turns through features in the pipe. These

values can then be combined with the heading angle to transform these linear distances in the robot fixed framed into the pipe coordinate frame. This allows for the position of the robot within the pipe to be obtained. It is important to note that the accuracy of the encoders will always be ± 1 count, however this will not always be the case for the linear distance. In the event the wheel slips, the encoder will still provide a count and cause the robot to think it has travelled when in reality it has not. Therefore, a no-slip assumption is key to the accuracy of this method.

3.3.3 Robot Control

In order to control the robot, it must possess some sort of onboard computer. For small electronics and robotics these are called microcontrollers, and they come in a variety of sizes, capabilities, and power requirements. Perhaps the most popular, are the Arduino family of microcontrollers because they are open source, low cost, and offer excellent performance. Also, because of the popularity of Arduino boards there are a large number of third party accessories, add-ons, and code libraries already available. For these reasons, it was decided to use an Arduino microcontroller, specifically the Arduino Uno (shown in Figure 3-17). The Uno offers a nearly perfect pinout to be used with a small robot. It features 14 digital I/O pins, 6 analog pins, a real time clock, and serial communication, all in a small, energy efficient board. The digital pins are needed to control the motors, and collect data from the accelerometer and encoders. The analog pins provide a way to directly read the voltage levels of each of the four pressure sensors to be used in the navigation system. It should be noted that depending on the final piezoelectric selection,

a voltage divider may be necessary to lower the voltages to levels readable by the Arduino (0-5V).
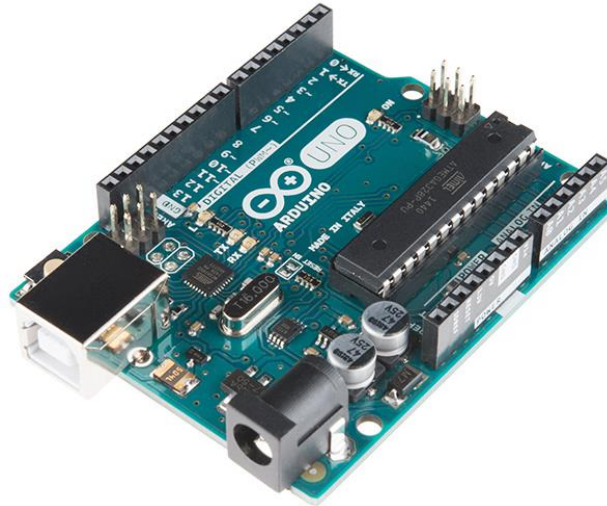
Figure 3-17: Arduino Uno R3 [30].

Besides the microcontroller, there are many other devices needed ranging from voltage regulator, motor driver, additional I/O ports, accelerometer, and adapters for other hardware. In robotics it is common to lump nearly all of these things onto a single circuit board called a shield. The shield essentially acts as an interface between all the sensors, power supply, motors, and the microcontroller. There are a wide variety of third party shields that have been designed to be compatible with the Arduino Uno, but it is often difficult to find a perfect solution, since not every project requires the same things. This means there are typically two options: 1) go with the closest match and build around it, or 2) create a custom shield specific to your needs. In this case it was decided to go with option 1, because the development of a custom circuit board with all necessary components was outside the scope of current work.

3.3.4 Conclusion

A navigation solution was proposed using a combination of a 3-axis accelerometer, 2 optical encoders, and 4 piezoelectric pressure sensors. The combination of these three sensor types allows for the robot position, velocity, and orientation to be determined with respect to the three main coordinate systems (inertial, pipe, and robot fixed). A summary of this solution, including sensor use, is shown in Table 4.

Table 4: Navigation solution summary.

State Variable		Use of Variable	Sensors Used
$\vec{x}$	x	Map location within pipe	Accelerometer, encoders & piezo pressure sensors
	y		
	z		
$\dot{\vec{x}}$	$\dot{x}$	Determine and control velocity of robot	Encoders & piezo pressure sensors
	$\dot{y}$		
	$\dot{z}$		
$\ddot{\vec{x}}$	$\ddot{x}$	Determine linear accelerations and solve for pitch and roll angles	Accelerometer
	$\ddot{y}$		
	$\ddot{z}$		
θ		Robot/pipe inclination angle	Accelerometer
ψ		Robot circumferential position	Accelerometer
β		Robot heading in pipe	Piezo pressure sensors

The viability of part of this solution was tested using a Pololu Zumo 32U4 robot which was equipped with a pair of encoders and a LSM303D accelerometer. Programs

were written in the Arduino IDE to have the robot display the pitch and roll angles, robot velocity, and distance travelled on a small LCD screen on the robot. These were only preliminary tests, but it showed a proof of concept and the capability of the controller to handle the needed computations. The use of the piezo pressure sensors to determine the yaw angle has yet to be tested using physical hardware and is purely theoretical at this time.

By using the accelerometer to take only instantaneous measurements, opposed to integrating these measurements, it essentially eliminates the issue of drift over time. However, this does not mean this method is without possible errors as most low cost MEMS sensors are known to have significant noise in their measurements. However, this issue can be addressed by using a filter, such as a low-pass or Kalman filter on the microcontroller. Filters are commonplace when it comes to navigation, especially autonomous navigation, and are well established tools used by controls engineers. The limitation of the robot to determine its position in the pipe is tied directly to the accuracy of the encoders, the analog voltage sensing capabilities of the controller, and the no slip assumption.

It was decided that an Arduino Uno microcontroller would be used as it offers a nearly perfect package of specs for small robotics usage. The Arduino Uno also has a plethora of 3rd party accessories and open source programs available making it a great option for an introductory robotics project. It is important to understand that electronics and computing technology is a rapidly changing industry with new products coming out

constantly. Therefore, in the future better performing, more efficient alternatives are likely to replace any hardware recommended here.

3.4 Communication

3.4.1 Introduction

There are many well established wireless communication methods such as those utilizing radio frequencies, acoustics, elastic waves, and optics. However, the fact that the intended operating environment is inside of a steel pipe limits the methods suitable to communicate through the pipe wall. The issue of communication between robots is a much clearer task that can be accomplished using one of the previously mentioned methods. However, since the robot will be inside of a live pipeline it is likely there will be an excess of noise which could cause significant signal interference when using acoustic methods. Also, the concept of using the pipe surface as a guide for elastic waves is a problem that is difficult to realize both theoretically and practically. Therefore, it was decided to focus on two different communication methods, optics and radio frequency (RF). In order to compare the two methods, the following criteria were used: 1) range, 2) data rates achievable, 3) energy consumption, 4) physical volume, and 5) reliability. The optimal choice for the purposes of this robot is one that has a higher range and data rate while possessing a smaller total energy consumption and physical volume.
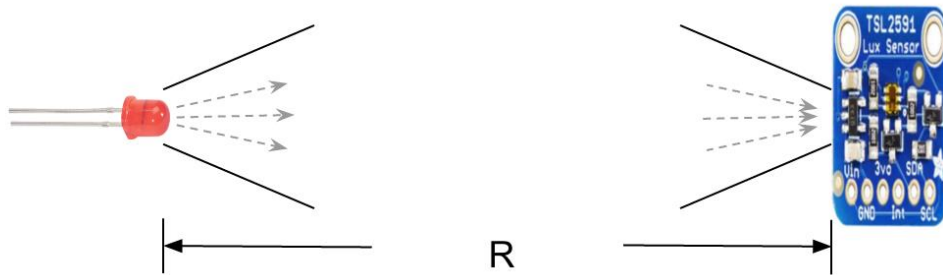
3.4.2 Optical Communication

Modern optical communication is typically achieved by using some sort of light to transmit an encoded message to an electronic receiver. This can be in the form of fiber optics, lasers, or simply a blinking light. Fiber optics is often the choice for robots that are

tethered as that tether provides a direct link between the two end points. However, the robot in this thesis is meant to be autonomous, meaning no tether. Using lasers for communication would require an advanced method of encoding/decoding messages sent and was thus considered outside the scope of this thesis. However, using blinking lights to transmit simple messages in some sort of communication scheme similar to Morse code or binary presented an attractive possibility. This was determined to be feasible since most transmission lines have infrequent blockage points meaning having line of sight between multiple robots is fairly likely. Also natural gas, even compressed gas, is a transparent fluid with optical properties similar to that of air. However, it should be noted that the transmittance, or a fluids effectiveness at transmitting energy through it, of Methane drops from nearly 100% to 50% in certain bands of the infrared spectrum [31]. Since natural gas is composed of ~95% methane, this means the use of instruments which rely on infrared light should be avoided as the drop in transmittance could cause signal loss.

When looking into possible hardware it was determined that a combination of LEDs and light sensors could provide a reliable, low power method to achieve optical communication. LEDs can be easily controlled to blink and in consequently send binary messages. A light sensor can be used on the other end to receive these light pulses which in turn can be read as binary by the microcontroller of the robot. This concept is illustrated in Figure 3-18. Using this combination, the performance of the system was determined by using the luminous intensity of the LED and the sensitivity of the light sensor. Luminous intensity is defined as the measure of luminous power in a particular direction from a light source and is given in units of candela (cd). Light sensors measure the amount of incident

47

light hitting the sensor area, or illuminance, and are often rated in terms of the range of illuminance they can detect. By knowing both the strength of the source and the lower limit of the sensor, the maximum range from which a sensor can detect a light source can be given as:

$$R\ [m] = \sqrt{\frac{Luminous\ Intensity\ [cd]}{Illuminance\ [lux]}} \tag{31}$$

Figure 3-18: Optical communication concept consisting of a LED and light sensor.

To determine the possible performance of this method two high performance light sensors and various strength LEDs were considered. For each LED and light sensor, the power consumption, physical size, and viewing angles were recorded. Note that in order to have the ability to transmit and receive signals in all directions a full 360° coverage is needed, meaning possibly multiple LEDs and light sensors per vehicle. Also different sensors have preferred operating wavelengths and therefore perform better when detecting a given color of light.

Table 5: Specs of the two light sensors considered.

Light Sensor	TSL2591	OPT3001
Dimensions (mm)	19 x 16 x 1	2 x 2 x 0.65
Minimum Lux	0.000188	0.01
Supply Current (mA)	275	0.0018
Field of View (°)	120	90
Preferred Color	red	yellow/green

3.4.3 Radio Frequency Communication

When considering using RF communications in metal pipes, there are two main factors to consider: operating frequency and signal attenuation. The fact that pipelines are hollow cylinders means that they serve as good wave guides to propagate EM waves along their longitudinal axis. However, the diameter of the pipe greatly influences the pipes ability to act as a wave guide depending on the frequency of the signal. If the frequency is too low for a given diameter, the wave paths will interfere with each other and cause a loss in strength of signal, or attenuation. However, if the frequency is sufficiently high, this will not happen. The breakpoint at which this happens is called the cutoff frequency. The cutoff frequency is determined primarily by the diameter of a pipe, but is also affected by the pipe material, material surrounding the pipe, and even depth that the pipe is buried. Extensive work has been done in the past to characterize the relationship between cutoff frequency and diameter of a metal pipe, an example of which is shown in Figure 3-19.
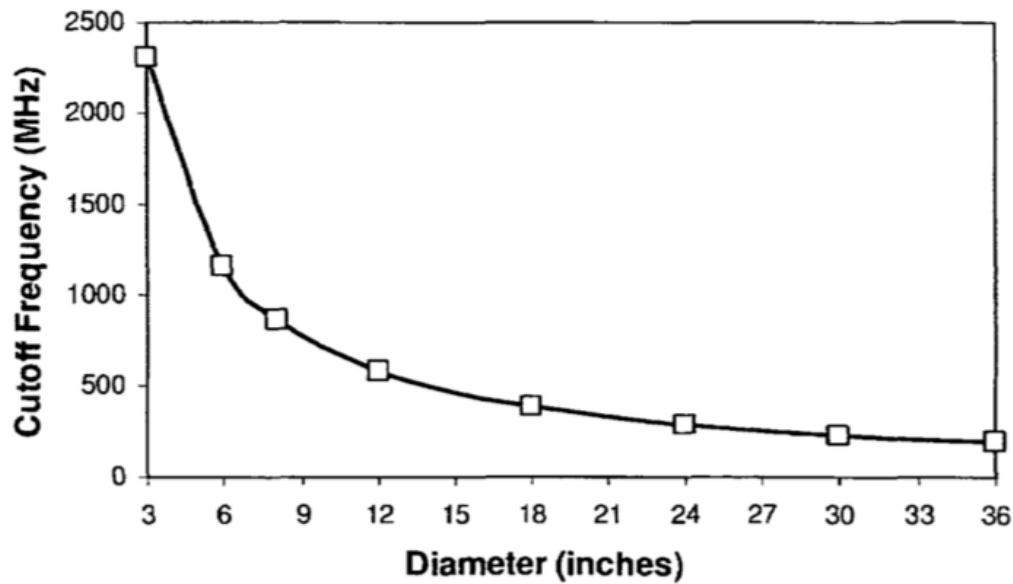
Figure 3-19: Cutoff frequency versus diameter for a metal pipe [32].

The effect of pipe features such as bends on signal attenuation is also important. If the signal cannot pass through these features, then it can severely limit the operational range of the antenna. Arumugam et al. studied the effect of pipe geometry and features such as bends and again a direct link to the cutoff frequency was found (see Figure 3-20).
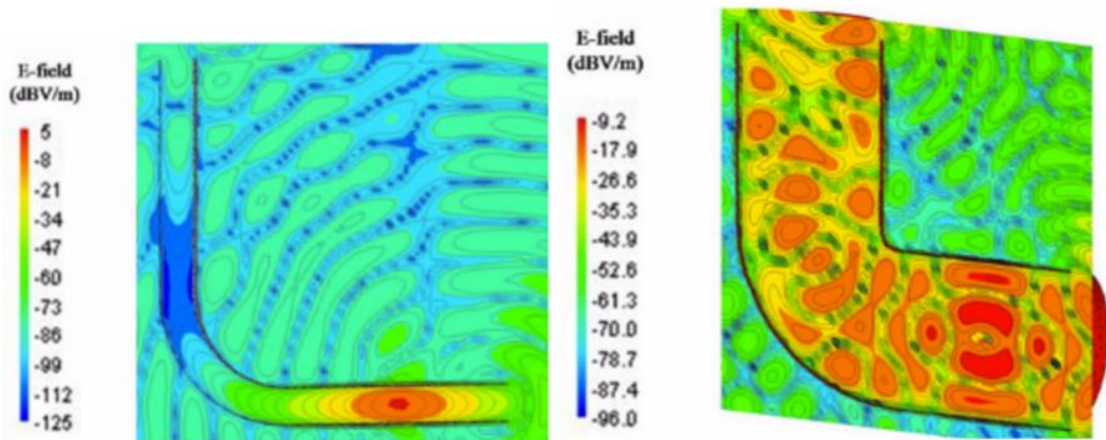
Figure 3-20: Illustration of the electric near field from a RF source in a bent pipe both below (left) and above (right) the cutoff frequency. Note the significant attenuation when operating below the cutoff frequency compared to operating above it. Images from [33].

Using this knowledge, it can be stated that the most important factor in choosing RF hardware is ensuring the operating frequency is above the cutoff frequency. Since the robot is meant to inspect transmission lines (typically > 12" diameter) this limit can be safely set at 1 GHz. When looking for hardware it was found that a strong candidate was the XBee family of radios from Digi. The XBee family are small radio transceivers which come in several different variations of communication protocol, operating frequency, antenna style, and antenna strength. The XBee products also use a single pinout that is compatible with many shields designed around using Arduino. An example XBee is shown in Figure 3-21.

Figure 3-21: XBee Pro 63 mW PCB antenna – Series 2B radio module.

The XBee would allow for a simple communication method as it can operate as a transmitter and receiver, meaning it could act as a mobile wireless node in point to point communication. A graphic of this concept is presented in Figure 3-22. It is also worth noting that RF communication is currently used by some smart pigs in industry, meaning there exists some sort of infrastructure in place to support communication with RF devices.

Therefore, the transceivers at either end of Figure 3-22 could be permanent antennas placed within the pipe, or other mobile nodes on other robots. This means that using RF communication it would be possible to not only communicate between multiple robots within the pipe, but also to outside base stations given the infrastructure exists.
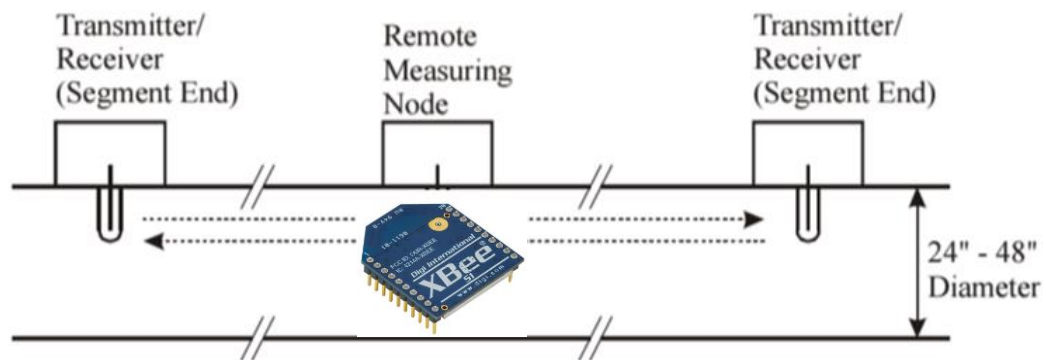
Figure 3-22: Example of using a wireless communication module in a pipe [34].

3.4.4 Conclusion

In order to compare the proposed optical and RF hardware setups a standard had to be set to calculate an estimated energy consumption. Therefore, it was decided that the communication system would be used to send a message in a 30 second window once every hour. This is a realistic scenario even during a mission due to the real time clock on the Arduino microcontroller. By simply sending a time stamp when transmitting a message, multiple robots can keep their clocks synchronized. Establishing this window also reduces the total energy consumption spent on communication, since in both cases the transmitters and receivers can go into a sleep mode where very minimal power is drawn ($\sim nW - \mu W$). Using this communication scheme the best hardware candidates were determined foe each method. These were a combination of 3 TSL2591 light sensors paired

with 3 5mm high flux red LEDs for optical, and the XBee Pro 63mW PCB antenna - Series

2B transceiver for RF. The specs of this XBee model are presented in Table 6.

Table 6: Specs for the XBee Pro 63mW PCB antenna – Series 2B.

Transmit Current (mA)	205
Receiving Current (mA)	47
Idle Current (µA)	3.5
Range	Up to 1 mile
Frequency (GHz)	2.4
Max Data Rate (kbps)	250

Based on the specs of the two different hardware setups the final values of range,

data rate, and energy consumption were calculated, and are shown in Table 7. While the

physical volume is not shown in this table, it can be stated that due to the fact that the

optical setup requires multiple LEDs and sensors to achieve full coverage, that it would

comprise a larger percentage of the volume of the robot than the single XBee transceiver.

Also, the reliability of the XBee is believed to be higher due to the fact that the optical

method requires near line of sight to function properly. There is also a high possibility that

the light sensor could perhaps see multiple light pulses from different sides and

misconstrue the message being sent. The fact that XBee radios operate on well-established

protocol standards gives it the edge in this regard.

Table 7: Comparison of optical and RF communication concepts

Criteria	TSL2591 + LEDs	XBee Pro-Series 2B
Range	Up to 561 ft	Up to 1 mile
Max Data Rate	17.9 kbps	250 kbps
Energy Consumption	15.7 J/hr	24.87 J/hr

Using the information presented it can be stated that communication via RF is the stronger alternative, as it edges optical in 4 of the 5 comparison categories. While the optical method does offer a lower power alternative, the level of both energy consumptions relative to the overall battery usage is very minimal (< 0.6% of battery usage per hour) compared to the energy hungry motors driving the robot. The fact that the communication scheme of opening a 30 second window every hour to send a message is the main reason why the RF energy is able to achieve such low levels. If the transceivers needed to be on nearly all the time, then it is likely that the battery drain would be quite significant and communication via blinking LEDs might be a viable contender.
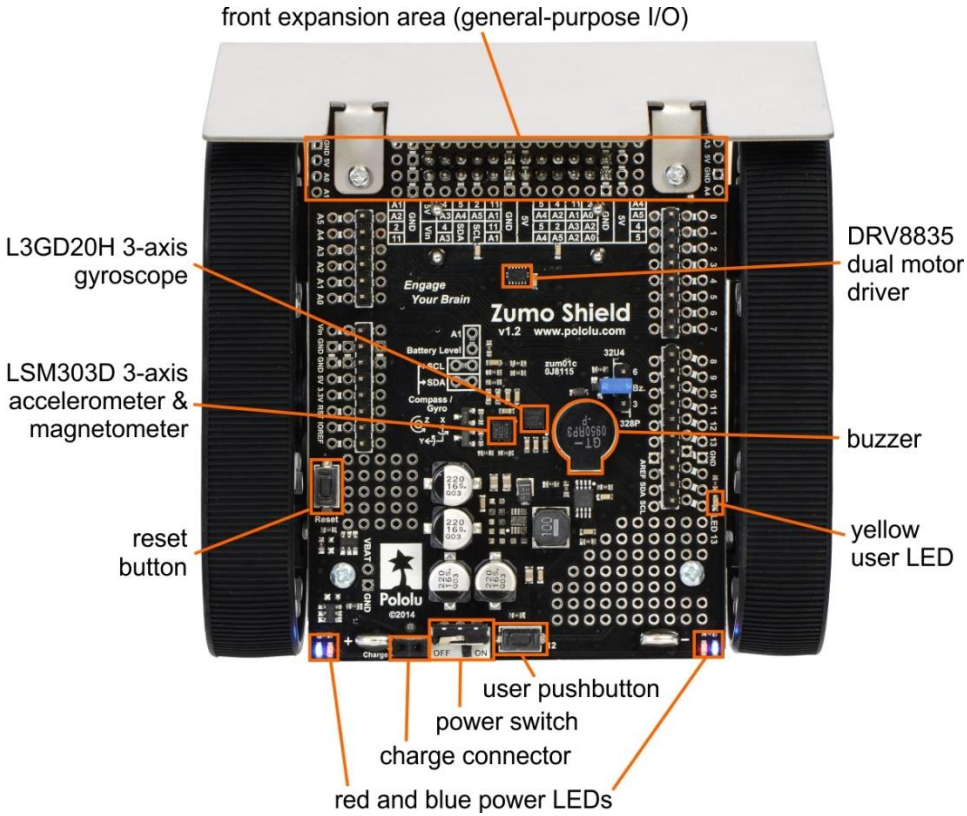
3.5 Robot Prototypes

This section details the parts used in the two prototype robots built. Many components were acquired off the shelf, but custom parts were created as needed. These parts were created in SOLIDWORKS and subsequently 3D printed in FullCure 720 transparent acrylic.

3.5.1 Prototype 1

The first robot prototype was based on the Pololu Zumo robot kit. The chassis, wheels, and shield from this kit were used. The Zumo shield for Arduino, v1.2 features an onboard voltage regulator, a DRV8835 motor driver (up to 1A per channel), and a LSM303D 3-axis accelerometer. This shield was used to interface with the Arduino Uno. The prototype used two 150:1 high power micro metal gearmotors for a front wheel differential drive. The Zumo chassis was originally intended to use 4 AA batteries, but was altered to house instead a 1000 mAh 2C battery pack and a 2" x 1" x ½ " N52

neodymium magnet. To account for this change a custom cover was made for the bottom of the battery box. This cover featured a slot sized for the magnet to avoid having the magnet move around within its compartment. This cover was designed to be screwed into the bottom of the robot. The energy harvesting system used in this prototype included a KidWind wind turbine generator and a 14 bucket conical turbine. A custom designed body was 3D printed to house all of the electronics and provide a more streamlined body to reduce the overall drag on the robot. The following series of figures show the different components of the first prototype.
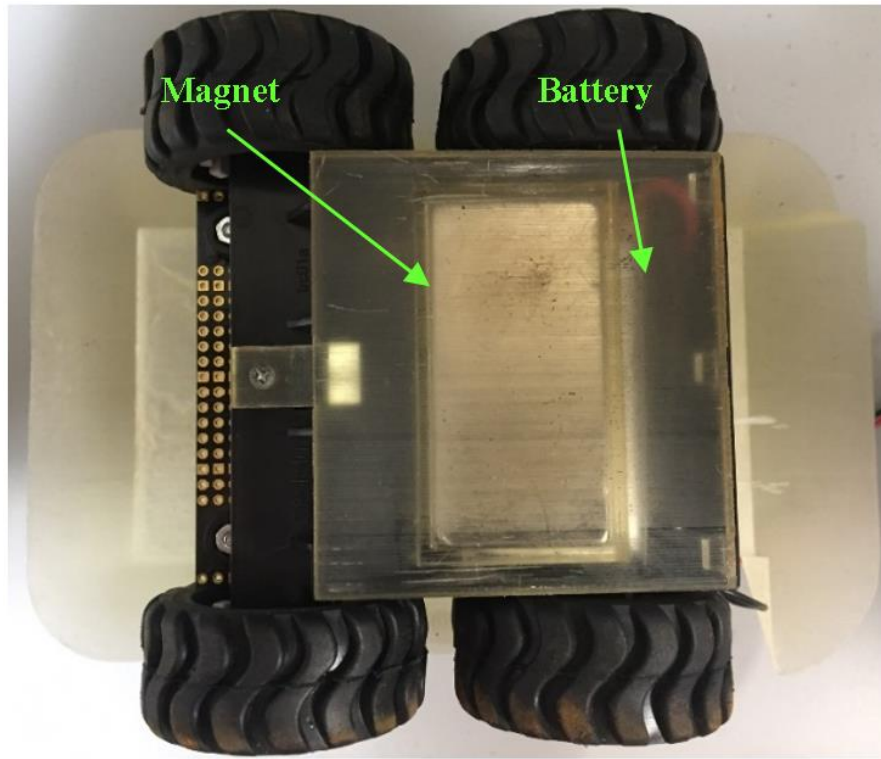

Figure 3-23: Layout of the Zumo shield v1.2 [35].
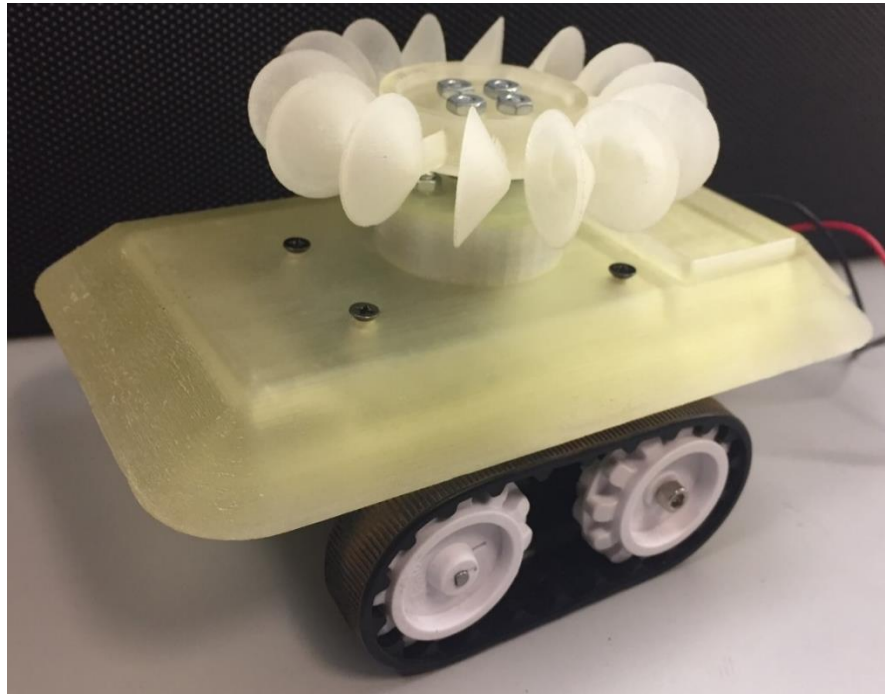
Figure 3-24: First robot prototype fully constructed.
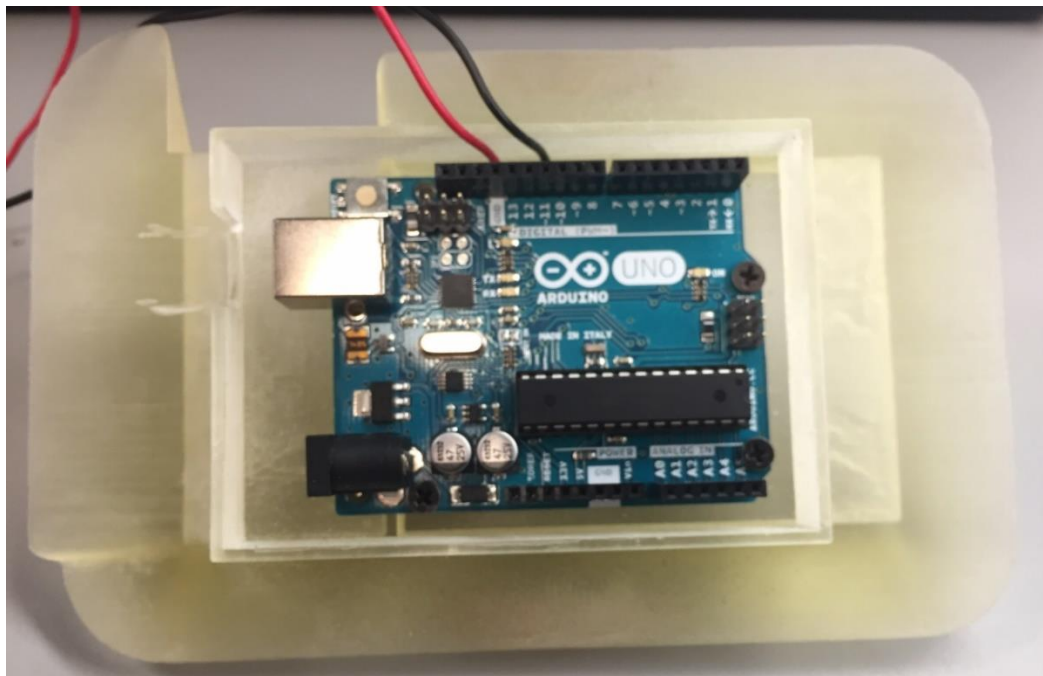
Figure 3-25: View of the underside of the robot body showing the Arduino.

Figure 3-26: View of the underside of the robot chassis showing the magnet, battery, and cover.

3.5.2 Prototype 2

The second robot prototype was designed to be a scaled down version of the first. This meant that several of the parts, namely the chassis and a mounting plate for the Arduino, had to be custom made. Also, the battery cover maintained the same design, just scaled down. The fact that this prototype was meant to be smaller meant that many of the electronics had to be swapped as well. The new electronics revolved around a new shield, the DFRobotShop Rover mobile robot shield. This shield features an integrated voltage regulator, LiPo charging chip, motor driver capable of up to 2A per channel, an XBee socket, and an analog pin expansion area. This shield does not contain an accelerometer,

but it does include a socket to use the newly selected XBee Pro-series 2B radio module and offers a smaller surface area compared to the original Zumo shield. The lack of accelerometer on the shield was made up by the newly available Arduino 101, which is an upgraded version of the Uno, that adds an IMU and Bluetooth connectivity. New, smaller 32mm wheels were used on this model. The same motors, 150:1 high power micro metal gearmotors, were used in the second prototype and had a pair of optical encoders mounted on them (3,000 counts per revolution of the wheel). The energy harvesting system also remained the same in this version, including a KidWind wind turbine generator and a 14 conical bucket turbine. The underside of the robot featured a smaller 700 mAh (20C) LiPo battery pack and a 2" x 1" x ¼" N52 neodymium magnet. Given the overall smaller size, a new custom body was created with more of a boxy design compared to the original. This body was created with angled corners to allow future placement of the piezoelectric pressure sensors that will be used in the navigation system. The following series of figures show custom parts and assemblies of the second prototype.
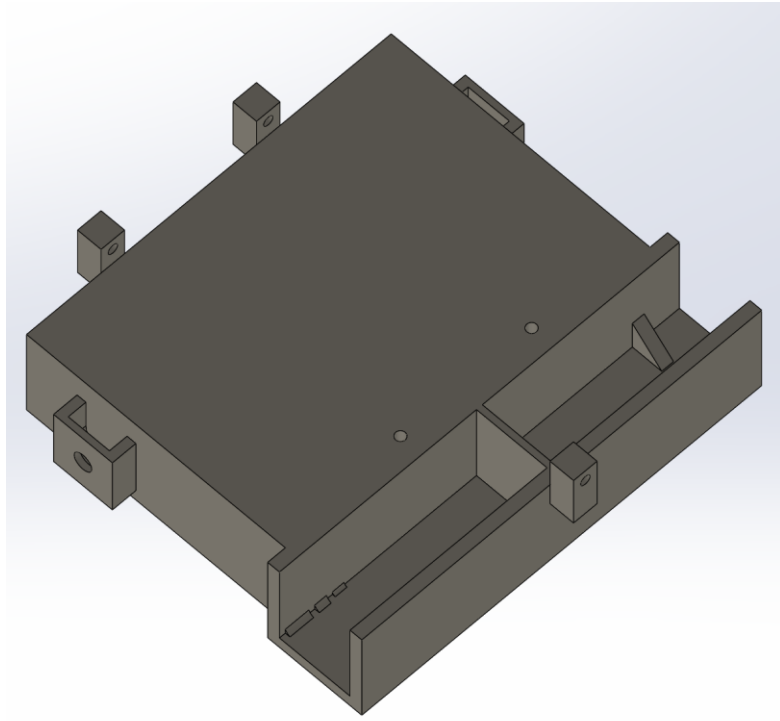
Figure 3-27: Custom designed robot chassis for the second prototype.
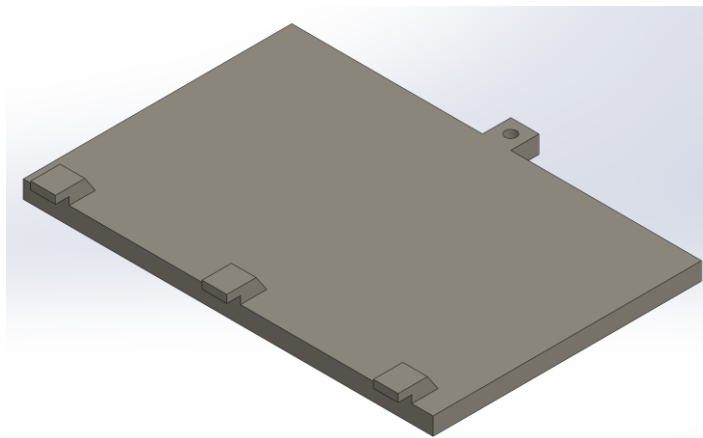
Figure 3-28: Scaled down battery box cover.
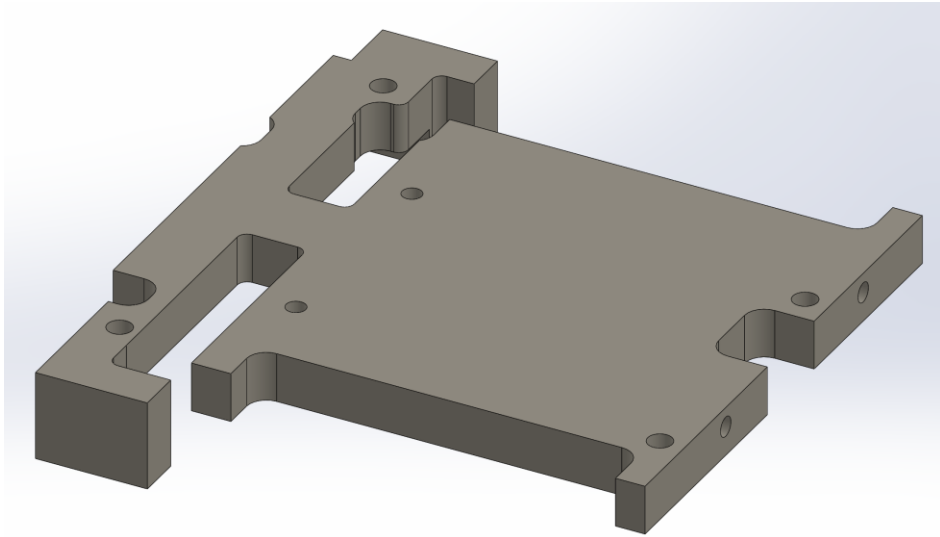
Figure 3-29: Custom Arduino mounting plate.
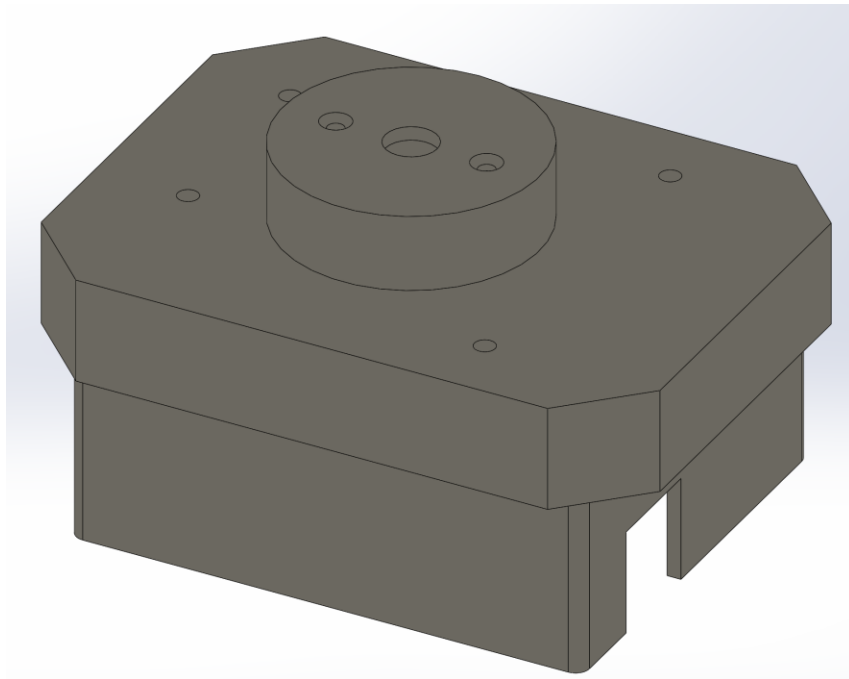
Figure 3-30: New robot body design featuring angled corners for future pressure sensor placement.
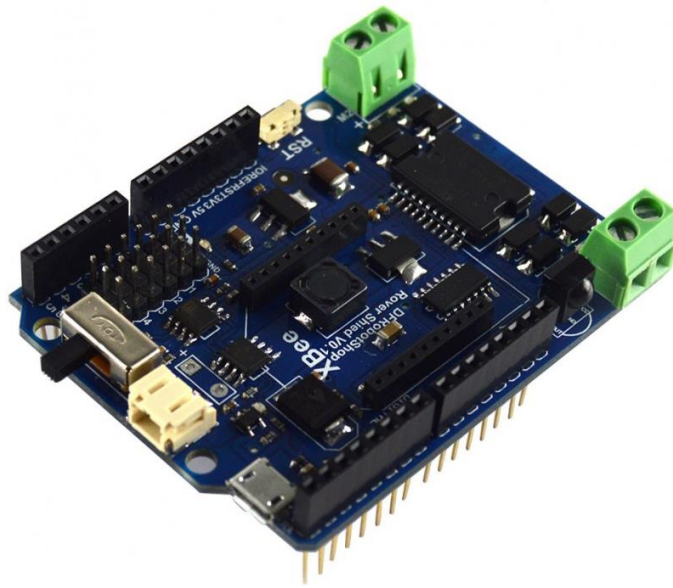
Figure 3-31: DFRobotShop Rover mobile robot shield.
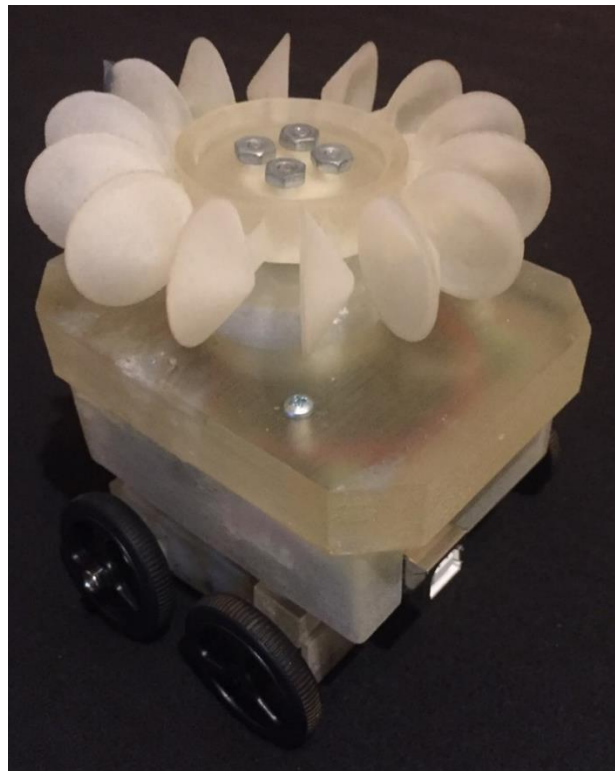
Figure 3-32: Fully assembled second prototype.

61
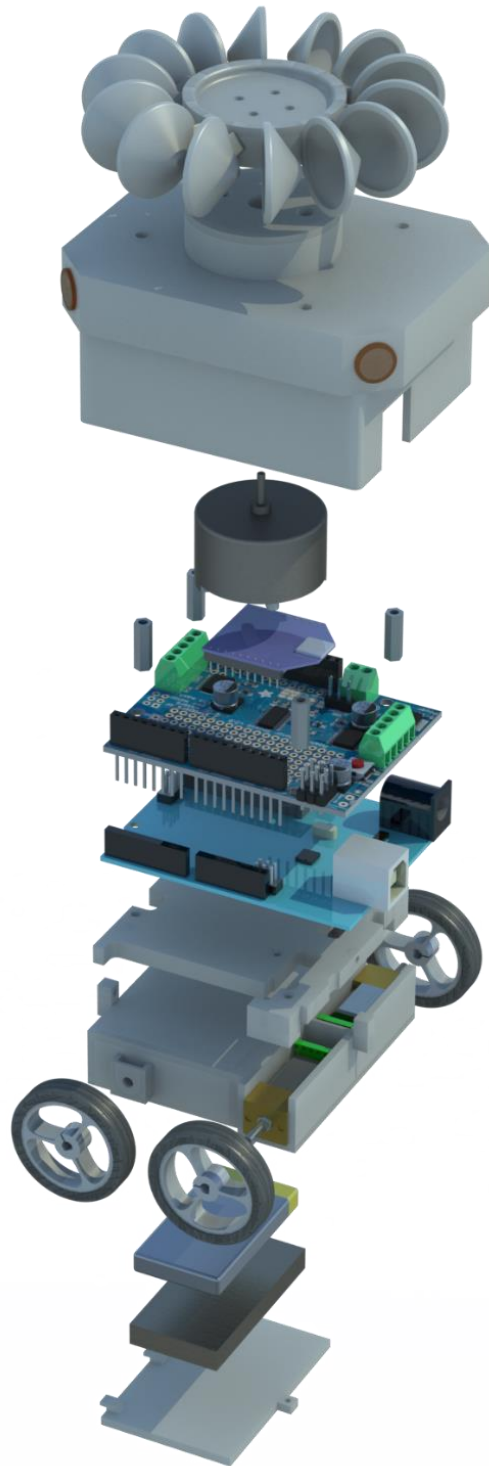
Figure 3-33: Exploded SOLIDWORKS assembly of the second prototype.
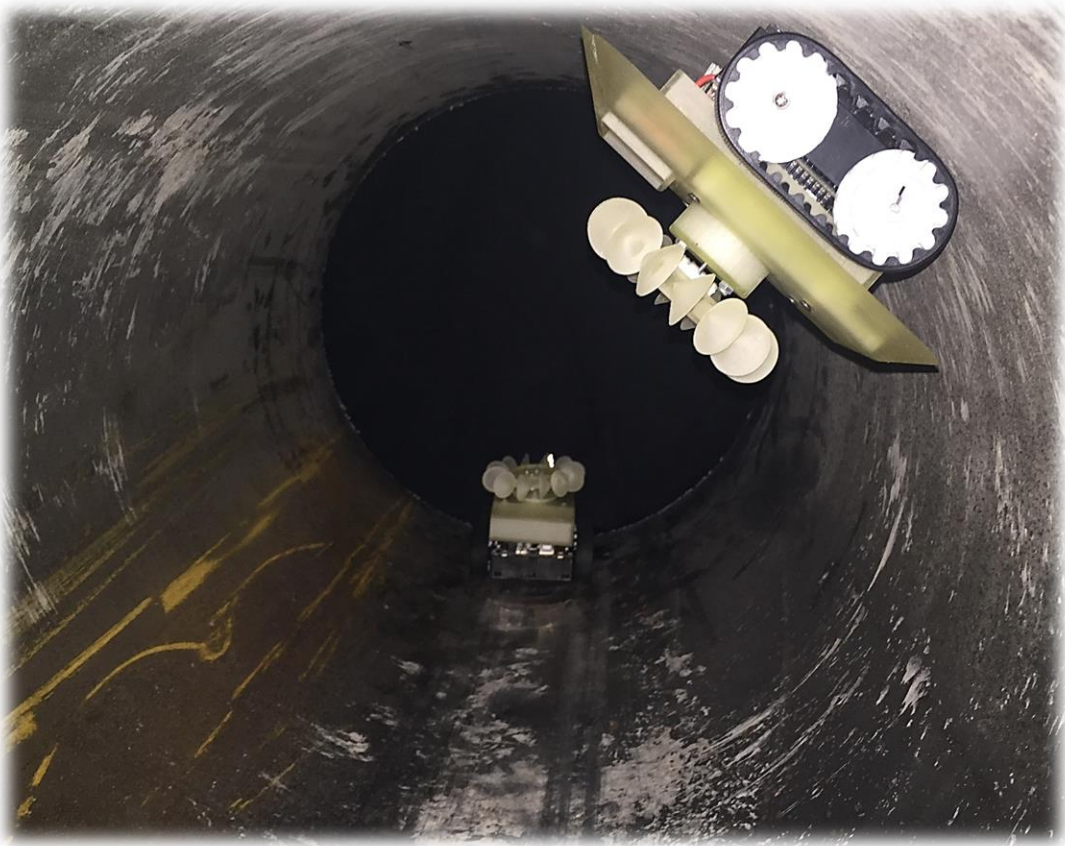
Figure 3-34: View of the first (top right) and second (center) robot prototypes inside a 16" pipe.

4. ENERGY HARVESTING EXPERIMENTS

4.1 Introduction

The goal of the energy harvesting system is to recharge the onboard batteries and as such it is important to show that a given system is capable of doing so. In order to test this several experiments were performed. First however, a method was needed to relate natural gas flow to air flow as working with natural gas has many safety issues. This was done by matching the power available in the lab environment to that of the pipeline environment to obtain a relationship between the speeds of each fluid type.

$$V_{air} = \sqrt[3]{\frac{\rho_{ng}}{\rho_{air}}} V_{ng} \tag{32}$$

In (32) $\rho_{ng}, \rho_{air}, V_{ng}$, and V_{air} are the densities and speeds of natural gas and air, respectively. It is important to note that the natural gas speed used in this expression is equivalent to the flow velocity at the turbine, or $\vec{V}_f(r_t)$. This relation was derived from (15) by acknowledging the fact that the physical energy harvesting system remains the same. By using this relation, it was determined that a wind tunnel could be used to replicate the expected conditions.

4.1.1 Experimental Setup

The general experimental setup shown in Figure 4-1 was used for most of the experiments performed. The setup consisted of the testing platform, a breadboard used to create circuits as needed, two NI MyDAQs for data acquisition, a flowmeter connected to a pitot tube mounted in the test section, and a computer running LabVIEW to record and analyze data. For each experiment performed the power output of the generator was

measured. This was done by taking analog measurements of voltage and current using a MyDAQ, from which the power can be expressed as

$$P_g = I\Phi, \tag{33}$$

where I and Φ are the current and voltage readings, respectively. The efficiency of the system is expressed as the ratio of the power generated and the power available in the fluid flow and is given as

$$\eta_{EH} = \frac{I\Phi}{0.5\rho A_t V^3}, \tag{34}$$

where ρ, V are the air density and speed inside the wind tunnel, respectively. Data points were recorded every $0.5 \, m/s$, with the first point being the cut-in speed. These two metrics, power generated and efficiency, were used to compare the sets of results.
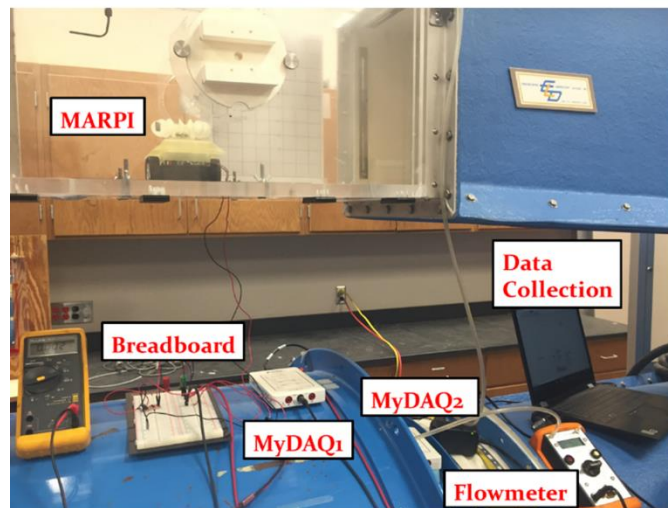
Figure 4-1: Experimental setup in the TAMU Aero department 1'x1' wind tunnel. Maximum tunnel velocity is 25 m/s.

4.2 Generator Selection

4.2.1 Methodology

In order to determine the best generator to use in the energy harvesting system, an experiment was designed to measure the voltage constant, K_V. This experiment used a drill to spin the motor/generator, a laser tachometer to measure the rotational speed, a multimeter to measure the voltage output, and another multimeter to measure the current passing through a 200 Ω resistor. The setup used, excluding the tachometer, is shown in Figure 4-2. Additionally, the generators were tested in the wind tunnel to measure the cut in speed, which is an effective way of measuring the level of torque required to begin harvesting energy.
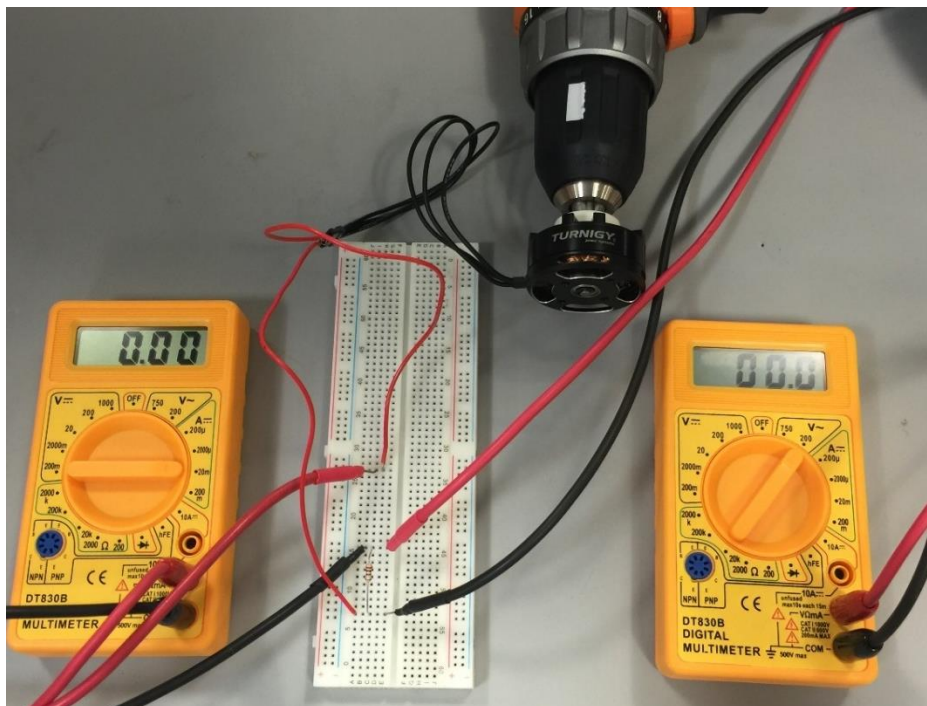
Figure 4-2: Experimental setup used to measure generator ratings.

During these tests, seven different DC motors/generators were tested (see Figure 4-3). These seven were chosen due to their relatively low advertised voltage constants and small sizes.
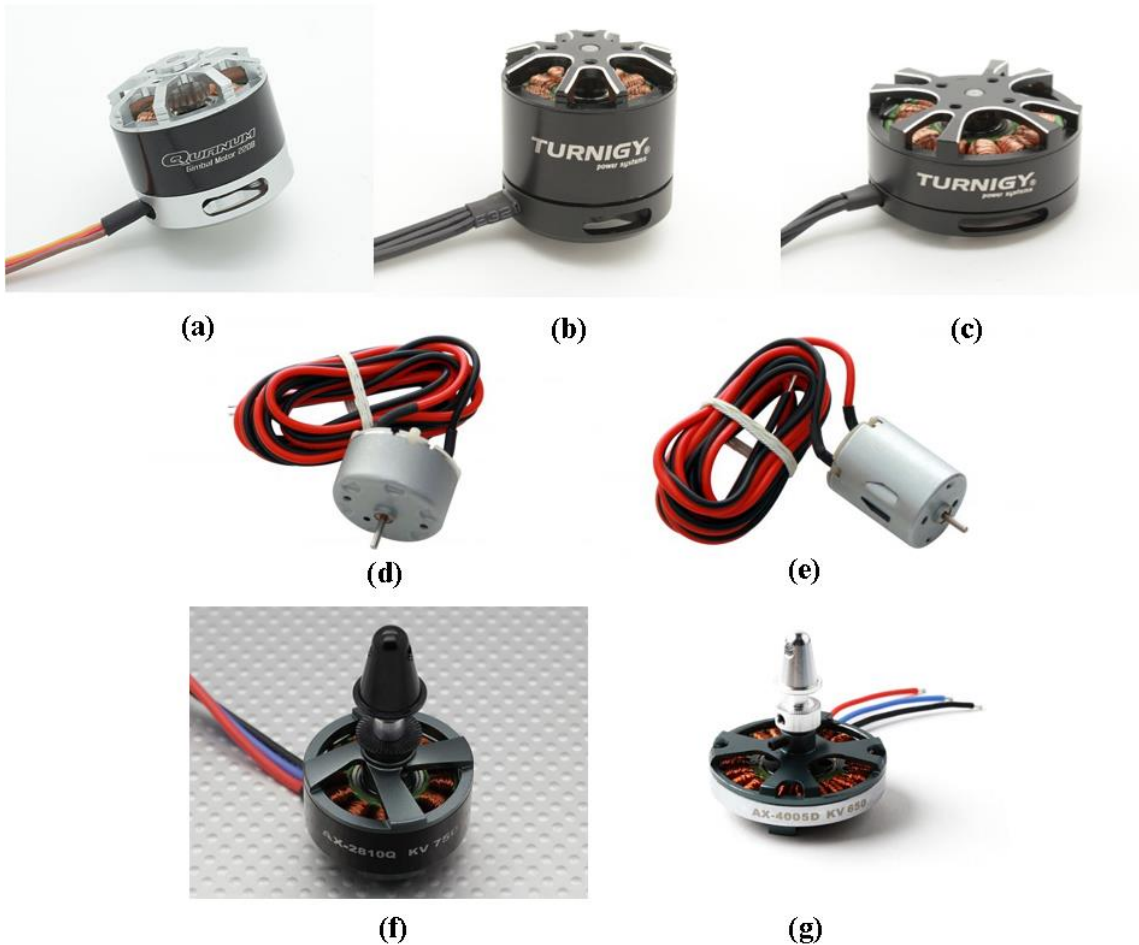
Figure 4-3: Different DC motors/generators tested: (a) Quanum 2208 gimbal motor (b) Turnigy HD 2212 gimbal motor (c) Turnigy HD 3508 gimbal motor (d) KidWind wind turbine generator (e) KidWind high torque wind turbine generator (f) AX 2810Q quadcopter motor (g) AX 4005 quadcopter motor

4.2.2 Results

When analyzing the results from this experiment (see Figure 4-4), it is clear that several generators, the Turnigy HD 3508 & 2212 and the Quanum 2208, produce a much higher voltage at the same rpm compared to others. Based on these results, the K_V values were determined from the slopes of the trendlines and are given in Table 8. While these three generators offer very low voltage constants, they are all classified as what is called an outrunner motor. This means that the outside casing of the motor itself spins around the windings as the shaft is spun, compared to inrunner motors where just the shaft spins inside the windings. This meant that it required more torque to begin spinning the shaft and generating any sort of energy output. This was confirmed in the wind tunnel as the cut in speed of all of the outrunner motors tested was either near or above the maximum flow speed achievable (25 m/s). However, the inrunner type motors tested, both of the KidWind generators, were able to achieve fairly low cut in speeds between 7-8 m/s in air. Using this information, it was decided that of the motors tested, the KidWind wind turbine generator was the best solution as it showed a good middle ground between low K_V ($454.5\ rpm/V$) and startup torque. The shaft of this generator is $10\ mm$ long and $2\ mm$ in diameter. This generator was used in all subsequent energy harvesting tests.
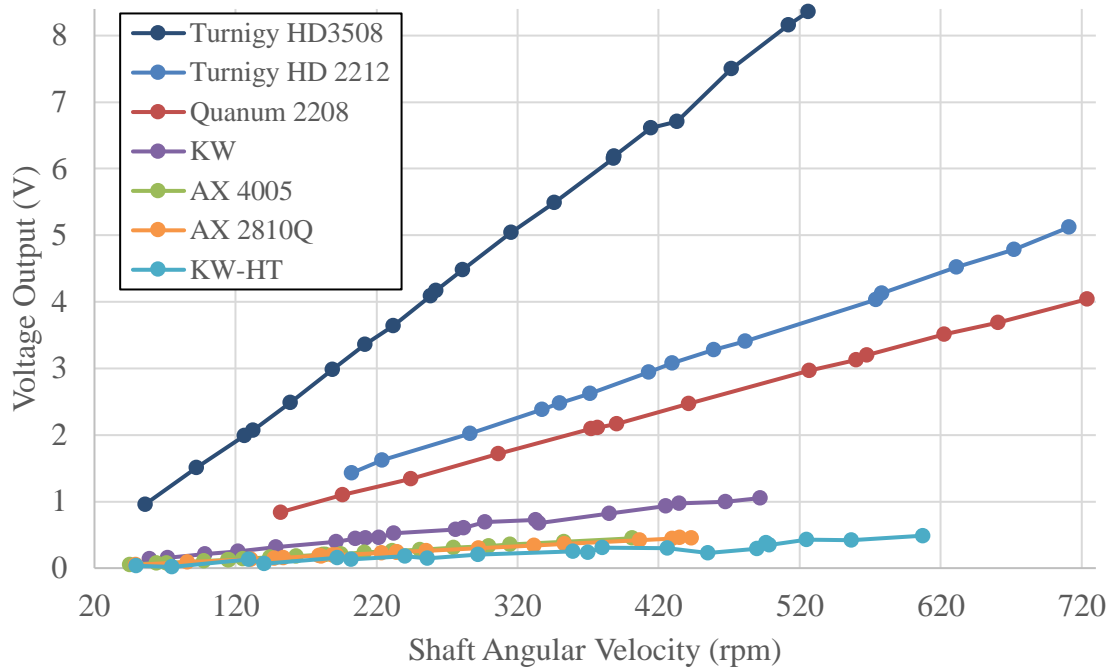
Figure 4-4: Experimental results of generator performance tests.

Table 8: Voltage constant values calculated for each generator tested.

Generator Tested	Voltage Constant, K_V (rpm/V)
Turnigy HD 3508	63.3
Turnigy HD 2212	138.9
Quanum 2208	178.6
KW	454.5
AX 4005	1000.0
AX 2810Q	1000.0
KW-HT	1250.0

4.3 Turbine Selection

4.3.1 Methodology

The first experiment performed was to determine the optimal turbine design from the given design space. Five unique turbine geometries were created using SolidWorks and are shown in Figure 4-5. For each geometry several variations were made by altering the

number of buckets/planes around the circumference of the turbine and subsequently 3D
printed.
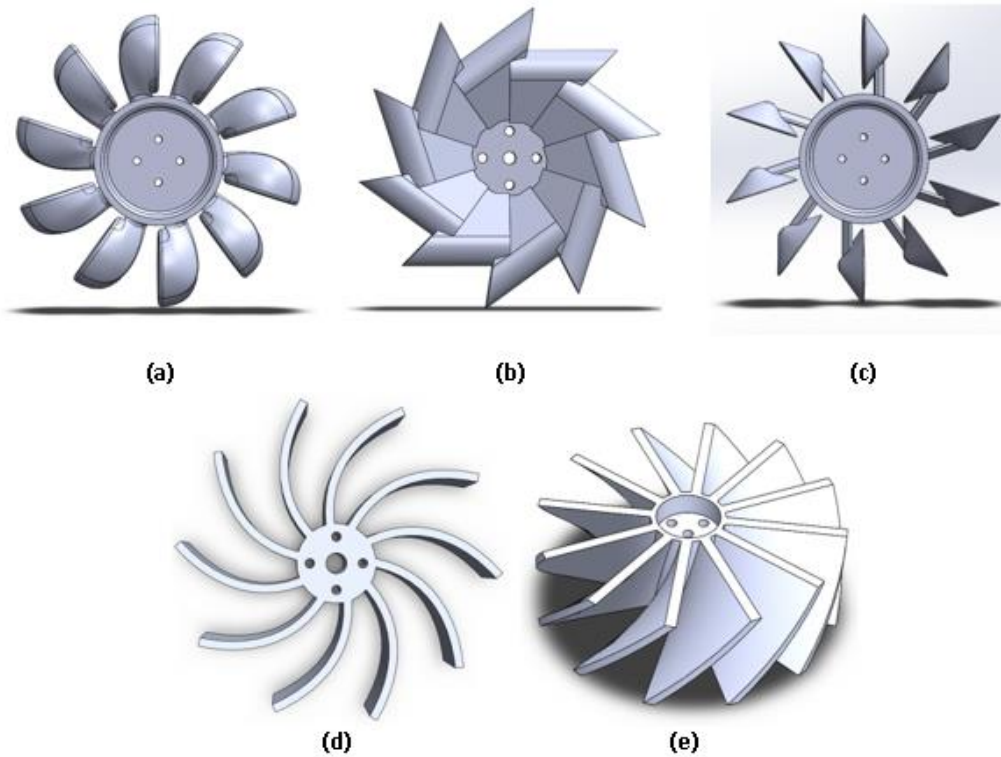
**Figure 4-5: Various turbine designs tested: (a) round buckets, (b) pinwheel,
(c) conical buckets, (d) curved planes, (e) angled planes.**

Each design was placed in the test stand shown in Figure 4-6, which consisted only
of the generator and turbine, and tested over the entire velocity range of the wind tunnel.

Figure 4-6: Test stand used to conduct experiments for turbine selection.

4.3.2 Results

During this experiment there were several telling results. First, is that two of the designs, the curved and angled planes, were unable to overcome the startup torque even at the maximum speed achievable in the wind tunnel (25 m/s air, ~9.4 m/s ng). Therefore, these two designs were considered to be unreliable to generate energy given the expected operating conditions (see Table 1). The pinwheel design was also ruled out as it had a cut in speed just below this maximum and due to the nature of the design and its size, the number of buckets could not be significantly increased to help capture more flow. The remaining two turbine designed were able to achieve cut in speeds near the expected minimum flow speed (~7 m/s air), which is promising as the goal is to be capable of constantly harvesting energy. The results from these tests are shown in Figure 4-7.

71
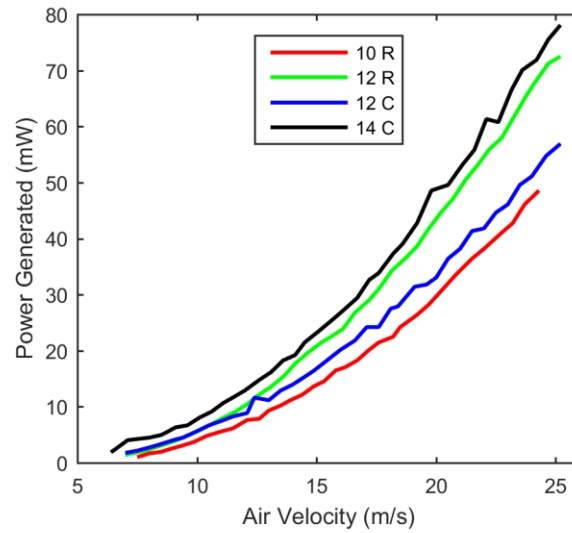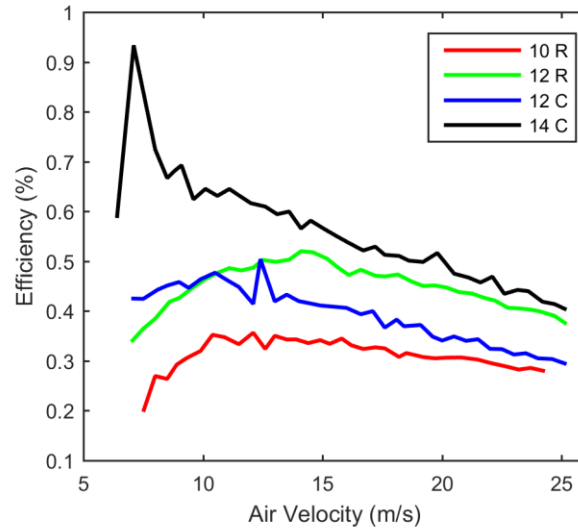
Figure 4-7: Results of turbine design experiments showing (a) power generated and (b) efficiency. Legend refers to number and shape of turbine buckets (R = Round, C = Conical).

It is clear that by increasing the number of buckets on the turbine the power generated and efficiency were increased. Consequently, the conical buckets presented the best option due to the fact that for a given turbine diameter, more buckets could be placed around the circumference without presenting a blockage to the one behind it. Also the

conical backside of the buckets reduces drag on the back side of the turbine effectively lowering the cut in speed due to a higher net torque.

4.4 Turbine Placement

4.4.1 Methodology

It is ideal to have some sort of body on the robot which can serve to house the electrical components and potentially reduce the drag coefficient, similar to the body of a car. As such the addition of this body must be taken into consideration during the design of the energy harvesting system. To account for this an experiment was performed to account for the placement of the turbine. To determine how far the turbine must be placed above the body of the robot, the distance, h, from the turbine to the body was increased from 5 mm to 11 mm in increments of 2 mm. The lower bound was set to ensure turbine clearance and the upper bound was set to 11 mm as going above this limit would contradict the idea of having a low profile robot. The test stand used for this experiment (Figure 4-8) was the same as that of the turbine selection tests but with an added mock body placed below the turbine. The KidWind wind turbine generator and 14 conical bucket turbine were used for these tests.
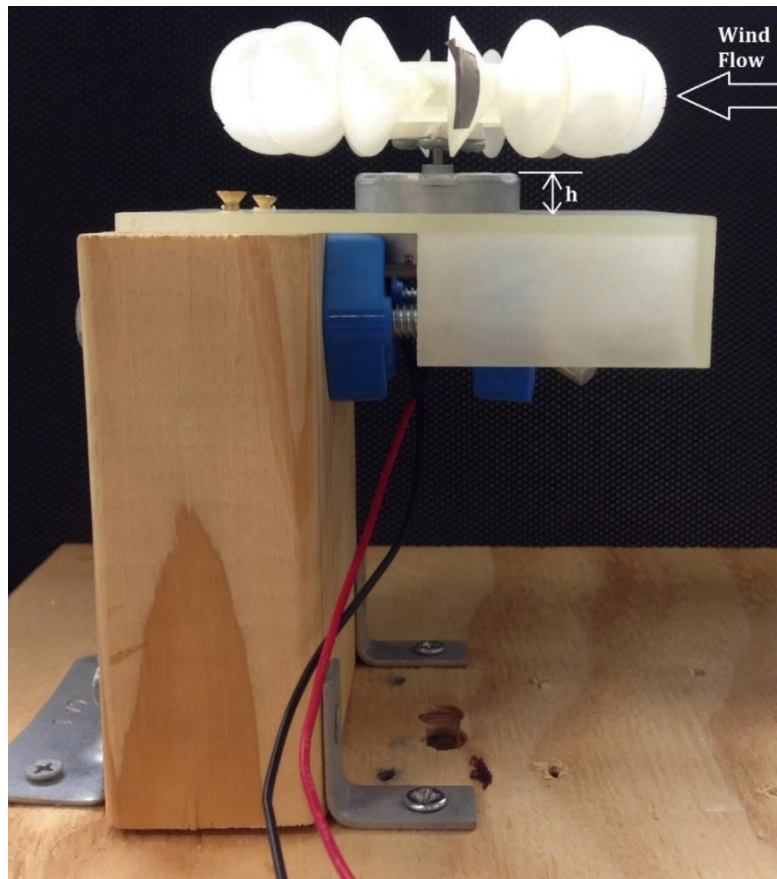
Figure 4-8: Test stand used to study effect of turbine height from body.

4.4.2 Results

It is clear from Figure 4-9 that giving the turbine more clearance above the body improves performance. What is interesting to note is that when comparing Figure 4-9 to Figure 4-7, both the levels of power generated and efficiency are decreased below 7 mm by the addition of a body below the turbine. This indicates that there are likely losses due to the boundary layer effect of the robot body on the flow. However, both the power and efficiency are improved above 7 mm. This shows that when the separation between the turbine and the body is large enough, the body helps to increase the flow rate into the turbine buckets.
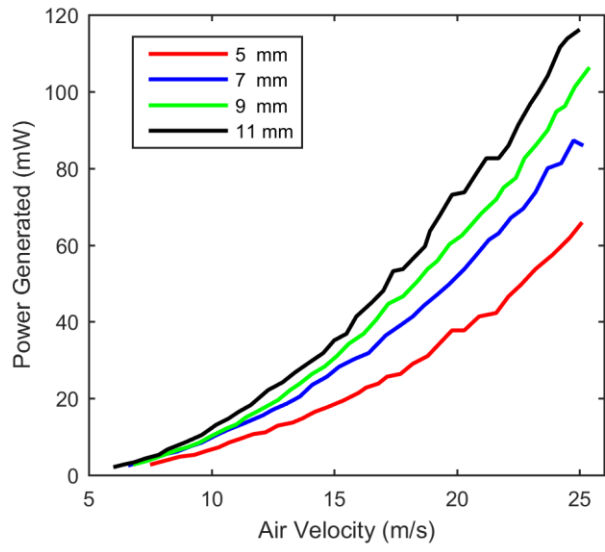
(a)
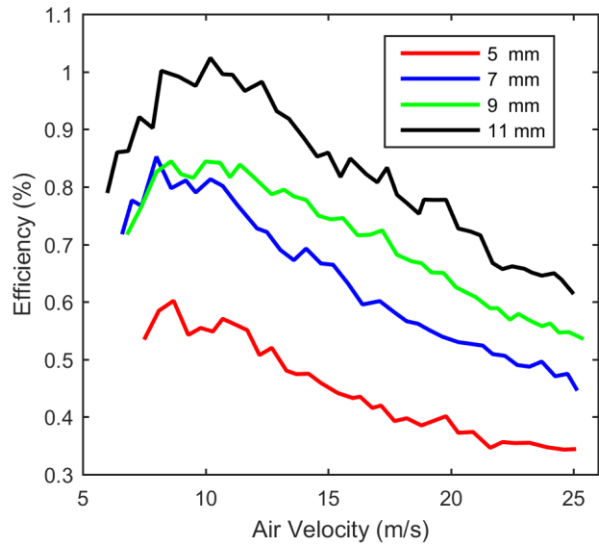
(b)

Figure 4-9: Results of turbine placement experiments showing (a) power generated and (b) efficiency.

5. ROBOT SCALING

5.1 Introduction

Being that a driving goal of this design is miniaturization, it is important to study

how the vehicle performance scales with size. Several cases were developed for this study:

1. All components can scale in all dimensions
2. Shield, microcontroller and charging circuitry do not scale in thickness
3. Case 2 + generator and motor do not scale in any dimension
4. Case 3 + shield, microcontroller and charging circuitry do not scale in any dimension
5. Case 3 + turbine does not scale in any dimension
6. Scale only battery capacity

The first case was chosen as a baseline to see the effects of scaling the entire vehicle. With

this baseline in place modifications were made in order of increasing complexity as it is

not entirely realistic that every component can scale. Case two was established as printed

circuit boards are already quite small in thickness and unlikely to be found or created with

a smaller out of plane dimension. Building on this is the availability of micro gear motors

and generators. Given that the robot must be capable of moving with or against live natural

gas flow sets constraints on the stall torque of the motor, and finding small motors capable

of handling such loads proved challenging. Similarly, the availability of a small generator

that can generate relatively high voltage at low torque and RPM values limits variability

in the selection process. These availability issues are the biggest contributors to the

development of cases 3-5. For case four it was further assumed that circuit boards of the

same capabilities at smaller sizes than the current one are hard to come by. Although it is

possible for the development of custom PCBs, this is outside of the scope of the current

work. It is clear from (15) that reducing the swept area of the turbine lowers the power

generated. To study what happens if the turbine size remained constant but the vehicle was allowed to scale lead to the development of case five. Finally, case six was established to analyze the effects of scaling only the battery on vehicle performance and design limits.

5.2 Methodology

For all scaling cases the following procedure was used. First the scaling factor, $\alpha \leq 1$, was applied to the length, width, and height of a component as shown below:

$$l_i' = \alpha l_i, \qquad w_i' = \alpha w_i, \qquad h_i' = \alpha h_i. \tag{35}$$

Using the new dimensions an updated projected area, volume and mass were found. This procedure was repeated for every component according to the scaling case being considered. Finally, the new total projected areas and mass were found for the vehicle. Using these new values in the governing equations yielded a new set of design parameters (11) & (14) and vehicle performance parameters (15), (17)-(19) & (21)-(23). Following this procedure, a MATLAB code was developed using the prototype shown in Figure 3-24 as a baseline.

To allow comparison of the design and performance parameters there are a large number of variables that must be defined. The flow parameters and pipe size were taken from Table 1. Nominal values of density and viscosity were used while the flow speed was varied over the entire range given. Also the nominal voltage of the battery, depth of discharge limit, and coefficient of friction were held constant as these will not change with scaling. The drag coefficient, C_D, was approximated as that of a truck and held constant as the robot will retain an approximately self-similar profile when scaling. The robot

velocity, scaling case, scale factor, and orientation with respect to gravity are all independent variables, three of which must be defined to study their effects individually.
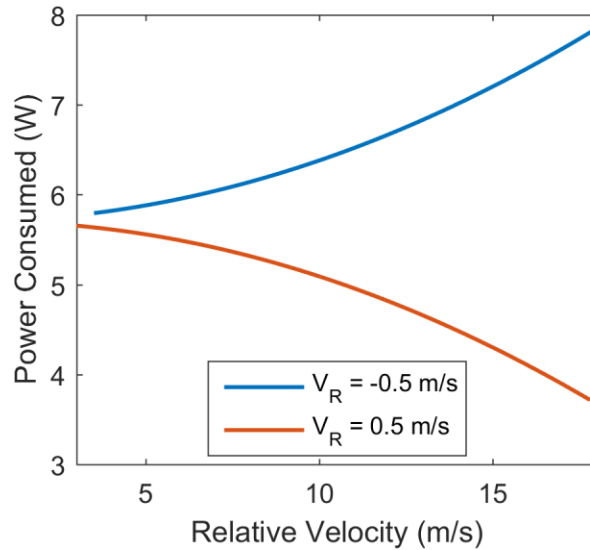
5.3 Scaling Limitations

During the scaling analysis presented here there are a few limits that needed to be considered in the design of a system. First is the fact that parts cannot interfere with each other. This was addressed by setting limits for the minimum chassis width when the motors are not allowed to scale. Additionally, the total current draw of the system cannot exceed the discharge rating of the battery. However, in practice, the discharge rate is not necessarily a limiting design point as LiPo batteries can be readily found with high discharge rates (~5-30 C_{batt}), meaning that a 1 Ah (5C) LiPo battery can discharge continuously at 5 A without harm. Similar to the total current draw, the motor current draw cannot exceed the limits of the motor driver. This is addressed by selecting a motor driver whose maximum per channel current is above the stall current of the chosen motors. Therefore, while performing the scaling analysis, the load torque placed on each motor was monitored to ensure the motors would not stall or exceed the current limitations.

5.4 Results

When comparing the design and performance parameters, there are quite a few conclusions that can be easily drawn from intuition and the governing equations. First, as the flow speed is increased the power generated and drag force increase. The increase in the drag force can be detrimental or helpful to the power consumed depending on if the robot is attempting to move against or with the flow, respectively. An example of this behavior can be seen in Figure 5-1. This difference is caused by the need of the motors to

78

either fight against drag or use the drag to help lessen the total load placed on them. This difference in power consumed corresponds directly to a change in the maximum run time and range of a full charge cycle. However, the ratio of P_g/P_c is increasing in both cases as $P_g \propto V_{rel}^3$ and $P_c \propto V_{rel}^2$, and as mentioned previously, the magnitude of V_{rel} is not changing much with respect to the robot velocity, V_R. Note that the definition of $V_{rel} = V_{f,c} - V_R$ is used for the x-axis in the following series of figures.

Figure 5-1: Comparison of power consumed for robot moving against ($V_R < 0$) and with ($V_R > 0$) the flow: $\theta = 0°, \alpha = 1, scaling\ case = 1.$

Naturally, the scaling case considered also has an impact on performance as each case introduces new limitations on the robot components. As the number of limitations is increased (increasing scaling case) the overall size of the robot is increased, for any $\alpha <$ 1. This means that the robot will effectively sit higher in the pipe and will experience a greater average velocity and velocity at the turbine. Therefore, both the power generated and power consumed will increase. However, there will be more available space for

additional battery capacity, meaning the maximum run time and range will increase. What

is less intuitive here is the effect of scaling case on the ratio P_g/P_c and therefore we turn

to the numerical implementation. Figure 5-2 shows that as the scaling case is increased

this ratio is marginally decreasing, with the exception of scaling case 5, which shows a

significant increase. In scaling case 5 the turbine remains a constant size while the robot

is allowed to shrink around it. This means that the incremental change of the radial position

of the turbine within the pipe is negligible compared to a change in area swept by the

turbine.
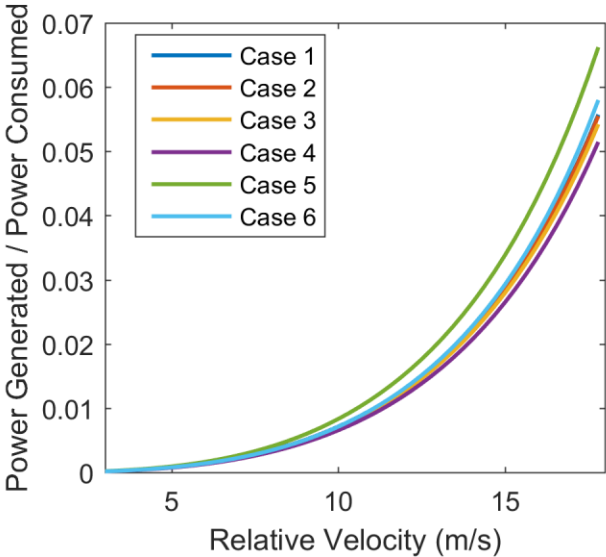
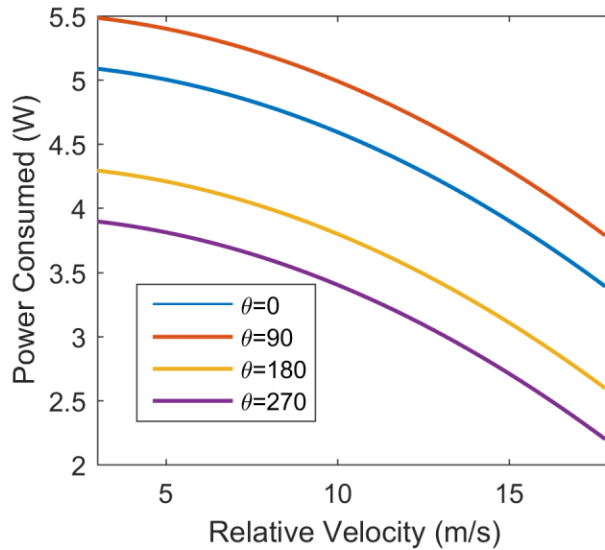**Figure 5-2: Comparison of P_g/P_c for various scaling cases: $V_R = 0.5\ m/s$, $\theta = 0°$, $\alpha = 0.9$.**
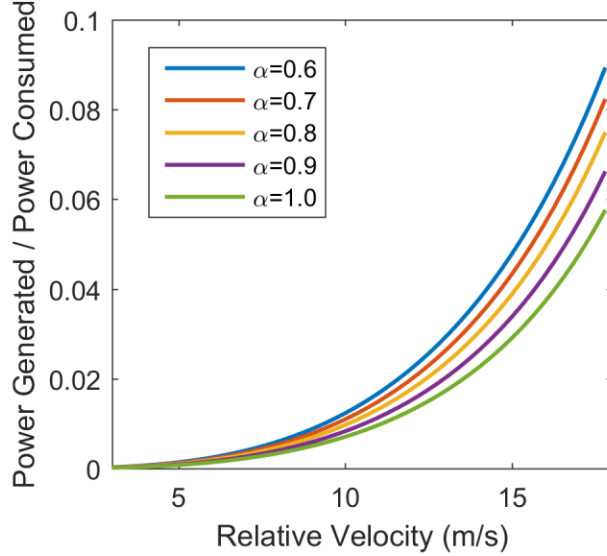
Figure 5-3: Comparison of P_g/P_c for various scale factors: $V_R = 0.5\ m/s\,, \theta = 0°, scaling\ case = 5.$

The effect of the scale factor, α, on vehicle performance and design is similar to that of the scaling case. As α is decreased, the robot is shrinking, meaning there is a smaller drag force and weight acting on it. These two facts combined mean there is a smaller load placed on the motors and therefore a lower power consumption. It also means that the magnetic force required, $F_{mag,R}$, is lower and the maximum allowable flow velocity, $V_{f,max}$, is increased. However, as the robot is shrinking there is less room to place batteries meaning the battery capacity is decreasing. Therefore, the maximum run time and range are lower. With the exception of scaling case 5 the turbine swept area is reducing meaning P_g is decreasing. It can be seen in Figure 5-3 that as the robot is allowed to continue shrinking around the turbine the ratio P_g/P_c is increased. However, the scaling limits must be considered, meaning that the robot must allow enough space to fit two motors capable of handling the load levels without stalling. Therefore, realizing a robot with a scale factor

81

of $\alpha < \sim 0.8$ is not possible without finding alternative smaller capable motors, which as mentioned previously has been unfruitful.

Lastly, the effect of the robots orientation with respect to gravity on vehicle performance was analyzed. To do this, angle values of multiples of 90° were substituted into (12) as these will correspond to the extremes of the performance parameters. Figure 5-4 shows that if the robot is moving in the direction of the fluid flow ($V_R > 0$) that the preferred orientation to minimize power consumed is $\theta = 270°$. In the case that the robot is travelling against the flow this minimum occurs when $\theta = 90°$. However, since it is not realistic to assume that the robot can always travel vertically since vertical pipes are not very common, the next best alternative in both cases is $\theta = 180°$. This means that the robot should travel on the top of the pipe to minimize power consumed. While this is not necessarily intuitive, it is a direct consequence of the design requirement that $F_{mag} = F_{mag,R}$ and therefore when the weight cancels out as much of the magnetic force as possible the loading on the motors is minimized.

Figure 5-4: Comparison of power consumed for various inclination angles: $V_R = 0.5\frac{m}{s}, \alpha = 0.8, scaling\ case = 5.$

The results up to this point show that to minimize power consumption travel with the flow ($V_R > 0$) at either $\theta = 270°\ or\ \theta = 180°$, and to maximize range per unit charge time to maintain a large turbine area while having a smaller robot (case 5). These results were the basis of creating the second robot prototype, and therefore we should quantify several of its performance parameters as a function of size. First is the maximum run time and range, shown in Figure 5-5 and Figure 5-6, respectively. It is clear from these results that both of these parameters decrease as the robot shrinks. This is because the total energy available is decreasing as the maximum battery size decreases. However, it was noted earlier that for scaling case 5, the extra range gained per unit charge time increases as the robot shrinks. Therefore, it is interesting to look at not only the run time and range on just one charge, but also the maximum range the robot can travel in a one day period. This is shown in Figure 5-7. Comparing the range per day values to those of the maximum range,

it is clear that for the given conditions the robot goes through ~3 run/charge cycles in a day. Now, the recharge time is ultimately dependent on the flow speed in the pipe, but what can be seen in Figure 5-7 is the fact that the range per day is higher for a smaller robot. Again, the commercial availability of hardware, specifically smaller, capable motors and generators, is limited and therefore realizing a fully functional robot smaller than $\alpha = 0.8$ is not feasible without the creation of new custom parts.
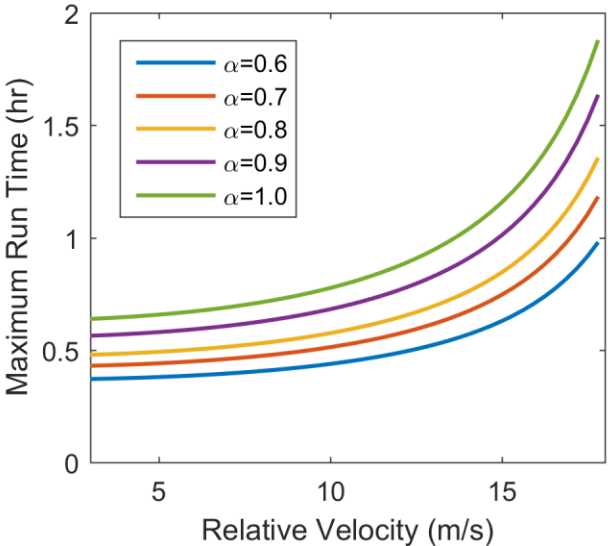
Figure 5-5: Maximum run time as a function of scale factor. $V_R = 0.5\frac{m}{s}$, $\theta = 180°$, $scaling\ case = 5$.
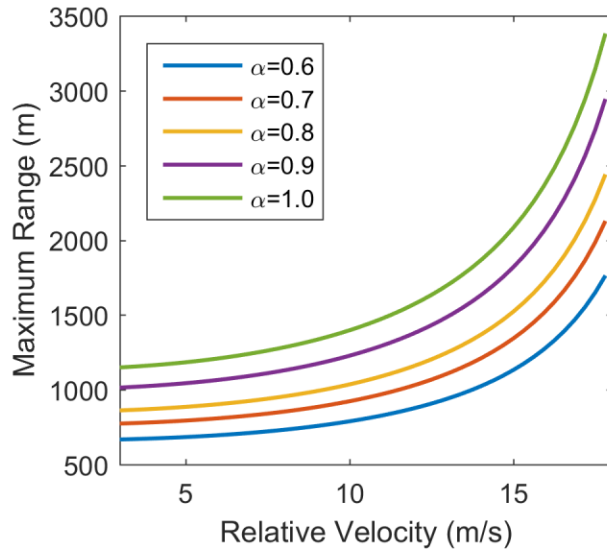
Figure 5-6: Maximum range as a function of scale factor. $V_R = 0.5 \, m/s$, $\theta = 180°$, $scaling \, case = 5.$
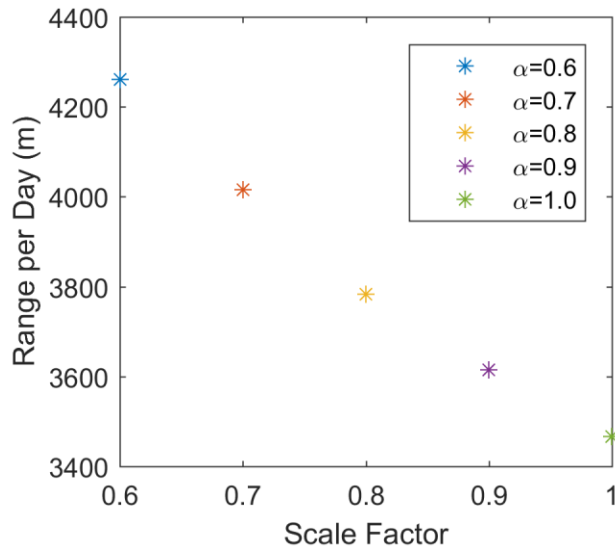
Figure 5-7: Range per day as a function of scale factor. $V_f = 12 \, \frac{m}{s}$, $V_R = 0.5 \, \frac{m}{s}$, $\theta = 180°$, $scaling \, case = 5.$

When studying the purest form of scaling (case 1, which assumes every component on the robot can scale), a similar set of results for the maximum run time and range are

obtained (Figure 5-8 and Figure 5-9, respectively). When looking at the range per day, Figure 5-10, it now shows that the range per day is $\propto \sqrt{\alpha}$, rather than being $\propto 1/\alpha$, like in Figure 5-7. This point suggests that maintaining a large turbine area relative to the robot size allows it to carry out inspection missions for a longer duration and range per day.

Figure 5-8: Maximum run time as a function of scale factor. $V_R = 0.5 \frac{m}{s}$, $\theta = 180°$, $scaling\ case = 1$.

Figure 5-9: Maximum range as a function of scale factor. $V_R = 0.5\ m/s$, $\theta = 180°$, $scaling\ case = 1$.
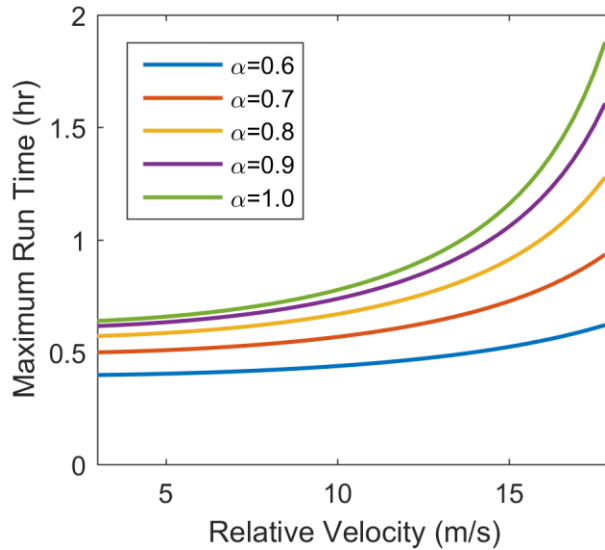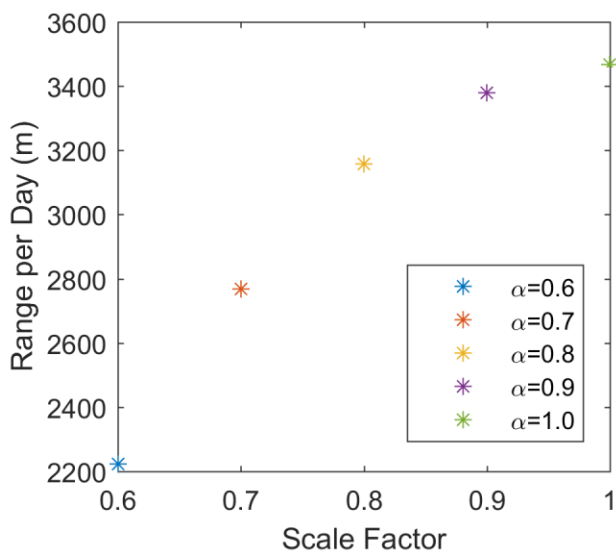

Figure 5-10: Range per day as a function of scale factor. $V_f = 12\ \frac{m}{s}$, $V_R = 0.5\ \frac{m}{s}$, $\theta = 180°$, $scaling\ case = 1$.
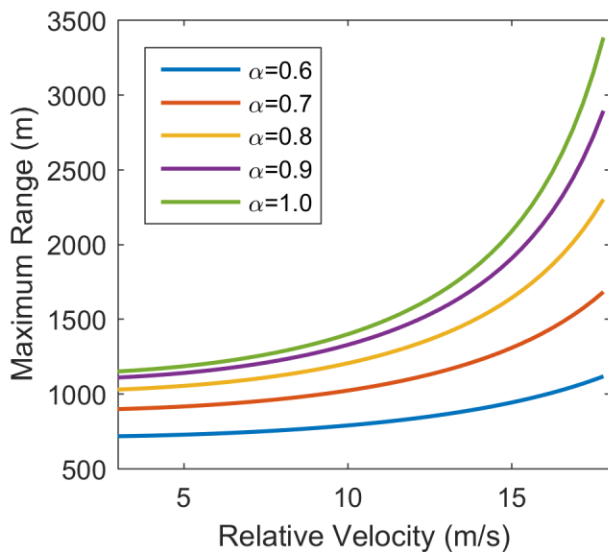
6. CONCLUSION

6.1 Conclusions

A model was developed to establish design requirements and performance metrics of a mobile pipe robot. The different subsystems required in this robot were reviewed and hardware chosen to create two different prototypes. Experiments were performed to validate that the energy harvesting system is capable of generating sufficient power for the charging of an onboard LiPo battery pack. A scaling analysis was performed to study the effects of scaling on the performance of the vehicle.

The energy harvesting system presented here has shown capable of generating enough power to recharge a LiPo battery pack under expected natural gas flow conditions. The system is also supportive in achieving the overall goals of minimizing robot profile and flow interference and allows for omnidirectional energy harvesting. However, the results from the energy harvesting experiments show a relatively low level of power generated compared to the expected power consumption. Therefore, the robot will need to take periodic breaks where it enters an ultra-low power state while the batteries are recharging. The efficiency values are also quite low, but it is believed that with extensive use of CFD, the turbine and body design could be optimized to increase these values. However, this study is outside of the scope of current work and has not yet been pursued.

Based on the scaling analysis, several conclusions were drawn. In order to minimize power consumption, it is ideal to have a small robot travelling axially with the flow at $\theta \ or \ \psi = 180°$. In order to maximize P_g/P_c, and consequently range versus charge time, it is best to have a relatively large turbine on a small vehicle. It was also determined

that having a large turbine on a small robot helps to decrease the charge time and leads to a higher value of range per day that the robot can travel. While the results theoretically show that a smaller robot can improve performance, it should be noted that the physical hardware used can set a minimum size achievable to keep a fully functional robot. In this case, this is set by the driving motors and corresponds to $\alpha \cong 0.8$. Below this point, the commercial availability of small actuators able to handle the loads becomes a problem.

6.2 Future Work

Currently, there a number of subsystems that need further study before a truly autonomous robot can be realized. First of which is an autonomous navigation solution that can use only references available to the robot to fully determine the vehicle location and orientation in time. This will require the ability to fuse data from current sensors and new sensors, as needed, into an algorithm that can be used by the microcontroller. Also testing of the communication hardware inside of an actual pipeline will be needed before it can be said with certainty that it is a completely viable solution.

The inclusion of structural health monitoring sensors must also be explored. Current candidates include: a CMOS camera for visual inspection; pressure, temperature and humidity sensors for gas quality monitoring; and ultrasonic sensors for corrosion detection in the pipe walls. It is likely that the addition of all these new sensors will likely warrant the need to create a new custom shield or sensor breakout boards in order to maintain an overall small robot size.

Finally, further testing of the second prototype should be performed to verify the results from the scaling analysis presented in section 5.4.

REFERENCES

[1] Interstate Natural Gas Association of America, American Gas Association, "Report to the National Transportation Safety Board on Historical and Future Development of Advanced In-Line Inspection Platforms for Use is Gas Transmission Pipelines," 2012. [Online]. Available: https://www.aga.org/sites/default/files/report_to_the_ntsb_on_historical_and_future_development_of_advanced_ili_inspection_for_use_in_gas_transmission_pipelines.pdf.

[2] Fraser Engineering, "Pipeline Pigs (Types and Functions)," 29 August 2014. [Online]. Available: http://www.fraserengineering.com/blog/pipeline-pigs-types-and-functions/. [Accessed 2016].

[3] C. Mitchell, ""WOOO-PIG-SOOIE!" - The Business of Pipeline Integrity II," RBN Energy, LLC., 31 October 2013. [Online]. Available: https://rbnenergy.com/wooo-pig-sooie-the-business-of-pipeline-integrity-ii. [Accessed 2016].

[4] S.-g. Roh and H. R. Choi, "Differential-Drive In-Pipe Robot for Moving Inside Urban Gas Pipelines," *IEEE Transactions on Robotics,* vol. 21, no. 1, 2005.

[5] A. A. F. Nassiraei, Y. Kawamura, A. Ahrary, Y. Mikuriya and K. Ishii, "A New Approach to the Sewer Pipe Inspection: Fully Autonomous Mobile Robot "KANTARO"," in *IEEE Industrial Electronics*, Paris, 2006.

[6]   A. Brunete, J. E. Torres, M. Hernando and E. Gambao, "A 2 DoF Servomotor-based Module for Pipe Inspection Modular Micro-robots," in *IEEE/RSJ International Conference on Intelligent Robots and Systems*, Beijing, 2006.

[7]   Y.-S. Kwon and B.-J. Yi, "Design and Motion Planning of a Two-Module Collaborative Indoor Pipeline Inspection Robot," *IEEE Transactions on Robotics,* vol. 28, no. 3, pp. 681-696, 2012.

[8]   H. R. Choi and S.-g. Roh, "In-pipe Robot with Active Steering Capability for Moving Inside of Pipelines," in *Bioinspiration and Robotics Walking and Climbing Robots*, Intech, 2007, pp. 375-402.

[9]   H. M. Kim, J. S. Suh, Y. S. Choi, T. D. Trong, H. Moon, J. Koo, S. Ryew and H. R. Choi, "An In-pipe Robot with Multi-axial Differential Gear Mechanism," in *IEEE/RSJ International Conference on Intelligent Robots and Systems*, Tokyo, 2013.

[10]   G. C. Vradis and W. Leary, "Development of an Inspection Platform and a Suite of Sensors for Assessing Corrosion and Mechanical Damage on Unpiggable Transmission Mains," 2004. [Online]. Available: https://www.netl.doe.gov/File%20Library/Research/Oil-Gas/Natural%20Gas/NT41645-FG033104.PDF.

[11]   Pipetel Technologies Inc., "Technology," 2015. [Online]. Available: http://pipetelone.com/pipetel-technology/. [Accessed 2016].

[12] H. Schempf, E. Mutschler, A. Gavaert, G. Skoptsov and W. Crowley, "Visual and Nondestructive Evaluation Inspection of Live Gas Mains Using the Explorer Family of Pipe Robots," *Journal of Field Robotics,* vol. 27, no. 3, pp. 217-249, 2010.

[13] T. Oya and T. Okada, "Development of a steerable, wheel-type, in-pipe robot and its path planning," *Advanced Robotics,* vol. 19, no. 6, pp. 635-650, 2005.

[14] J.-H. Kim, "Design of a Fully Autonomous Mobile Pipeline Exploration Robot (FAMPER)," M.S. thesis, Dept. Comp. Sci., Louisiana State Univ., Baton Rouge, LA, 2008. [Online]. Available: http://etd.lsu.edu/docs/available/etd-11112008-121037/unrestricted/Jong-Hoon_Kim_Thesis.pdf.

[15] C. Jun, Z. Q. Deng and S. Jiang, "Study of Locomotion Control Characteristics for Six Wheels Driven In-pipe Robot," in *IEEE International Conference on Robotics and Biomimetics*, Shenyang, 2004.

[16] D. Lee, J. Park, D. Hyun, G. Yook and H.-s. Yang, "Novel Mechanisms and Simple Locomotion Strategies for an In-pipe Robot that can Inspect Various Pipe Types," *Mechanism and Machine Theory,* vol. 56, pp. 52-68, 2012.

[17] A. H. Heidari, M. Mehrandezh, H. Najjaran and R. Paranjape, "Design, Development, Dynamic Analysis, and Control of a Pipe Crawling Robot," in *Robotics 2010: Current and Futrue Challenges*, InTech, 2010, pp. 261-298.

[18] Y. Sabzehmeidani, M. Mailah, M. Hussein and A. R. Tavakolpour, "Intelligent Control and Modelling of a Micro Robot for In-pipe Application," *World Academy of Science, Engineering and Technology,* vol. 4, pp. 12-24, 2010.

[19] F. M. White, Fluid Mechanics, McGraw-Hill Inc., 1979.

[20] L. L. Menegaldo, M. Santos, G. A. N. Ferreira, R. G. Siqueira and L. Moscato, "SIRUS: A mobile robot for Floating Production Storage and Offloading (FPSO) ship hull inspection," in *IEEE International Workshop on Advanced Motion Control*, Trento, 2008.

[21] Honeybee Robotics, "Pipe Inspection Robot," Honeybee Robotics, [Online]. Available: http://www.honeybeerobotics.com/portfolio/pipe-inspection-robot/. [Accessed July 2016].

[22] F. Tache, W. Fischer, G. Caprari, R. Siegwart, R. Moser and F. Mondada, "Magnebike: A Magnetic Wheeled Robot with High Mobility for Inspecting Complex-Shaped Structures," *Journal of Field Robotics,* vol. 26, no. 5, pp. 453-476, 2009.

[23] Helical Robotics, "FerroTanker-20," [Online]. Available: http://www.helicalrobotics.com/FerroTanker-20. [Accessed July 2016].

[24] K&J Magnetics, Inc., "The Original K&J Magnet Calculator," [Online]. Available: http://www.kjmagnetics.com/calculator.asp. [Accessed 2016].

[25] V. Lobo, N. Mainsah, A. Banerjee and J. W. Kimball, "Design Feasibility of a Vortex Induced Vibration Based Hydro-Kinetic Energy Harvesting System," in *IEEE Green Technologies Conference*, Baton Rouge, 2011.

[26] J. J. Allen and A. J. Smits, "Energy Harvesting Eel," *Journal of Fluids and Structures,* vol. 15, pp. 629-640, 2001.

[27] D. A. Wang and H. H. Ko, "Piezoelectric energy harvesting from flow-induced vibration," *Journal of Micromechanics and Microengineering,* vol. 20, 2010.

[28] D. Wood, Small Wind Turbines: Analysis, Design, and Application, Springer, 2011.

[29] Pololu Robotics & Electronics, "Optical encoder pair kit for micro metal gearmotors, 5V," [Online]. Available: https://www.pololu.com/product/2590. [Accessed 2016].

[30] Sparkfun Electronics, "Arduino Uno - R3," [Online]. Available: https://www.sparkfun.com/products/11021. [Accessed 2016].

[31] Sense Air, "Methane," [Online]. Available: http://www.senseair.com/senseair/gases-applications/methane-ch4/. [Accessed 2016].

[32] A. Sabata and S. Brossia, "Remote monitoring of pipelines using wireless sensor network". United States of America Patent US 7,526,944 B2, 5 May 2009.

[33] D. D. Arumugam and D. W. Engels, "Chracterization of RF Propogation in Helical and Toroidal Metal Pipes for Passive RFID Systems," in *IEEE International Conference on RFID*, Las Vegas, 2008.

[34] K. T. Erickson, A. Miller, E. K. Stanek, C. H. Wu and S. Dunn-Norman, "Pipelines as Communication Network Links," 2005. [Online]. Available: https://www.netl.doe.gov/File%20Library/Research/Oil-Gas/Natural%20Gas/FG113004.pdf.

[35] Pololu Robotics & Electronics, "Zumo Shield for Arduino, v1.2," [Online]. Available: https://www.pololu.com/product/2508/pictures. [Accessed 2016].